Successful IL-12 cancer immunotherapy requires NK cell-derived CCL5 for anti-tumor DC-T cell crosstalk

Nicole Kirchhammer[1, 13], Marcel P Trefny[1#], Marina Natoli[1#], Dominik Brücher[2#], Sheena N Smith[2], Franziska Werner[1, 3], Victoria Koch[1], David Schreiner[4], Ewelina Bartoszek[5], Mélanie Buchi[1], Markus Schmid[2, 6], Daniel Breu[2, 7], K Patricia Hartmann[2], Polina Zaytseva[2, 8], Daniela S Thommen[9], Heinz Läubli[12], Michal A Stanczak[1, 10], Abhishek S Kashyap[1, 11], Andreas Plückthun[2], Alfred Zippelius[1, 10, 13, 14]

[1] Cancer Immunology, Department of Biomedicine, University and University Hospital Basel, 4031 Basel, Switzerland

[2] Department of Biochemistry, University of Zurich, 8057 Zurich, Switzerland

[3] Present address: Molecular Dermato-Oncology and Tumor Immunology, Department of Dermatology, General Hospital Vienna, 1090 Vienna, Austria

[4] Immune Cell Biology, Department of Biomedicine, University Hospital Basel, 4031 Basel, Switzerland

[5] Microscopy Core Facility, Department of Biomedicine, University Hospital Basel, 4031 Basel, Switzerland

[6] Present address: Roche Diagnostics GmbH, 82377 Penzberg, Germany

[7] Present address: Department of Immunology, University Hospital Zurich, 8091 Zurich, Switzerland

[8] Present address: Institute for regenerative medicine, University of Zurich, 8952 Schlieren, Switzerland

[9] Division of Molecular Oncology and Immunology, The Netherlands Cancer Institute, 1066 Amsterdam, The Netherland

[10] Present address: The Bloomberg-Kimmel Institute for Cancer Immunotherapy and Department of Oncology, Johns Hopkins University School of Medicine, Baltimore, MD 21287, USA

[11] Present address: Boehringer Ingelheim Pharmaceuticals, Inc., 6877 Ridgefield, USA

[12] Medical Oncology, University Hospital Basel, 4031 Basel, Switzerland

[#] Authors contributed equally

[13] Corresponding authors

[14] Lead contact

Abstract

Targeting T cells for cancer immunotherapy commonly fails to generate lasting tumor control. Harnessing additional orchestrators of the immune response against tumors may enhance and broaden clinical benefit. Here, we demonstrate that therapeutic targeting of the IFNγ-IL-12 pathway relies on the amplification of anti-tumoral DC-T cell crosstalk by NK cells. Utilizing an engineered adenoviral platform for paracrine delivery into the tumor microenvironment, we show that IL-12 enhances functional DC-CD8 T cell interactions to generate profound anti-tumor immunity. This effect depends on the abundance of intra-tumoral NK cells and specifically their capacity to produce the DC chemoattractant CCL5. Failure to respond to IL-12 and other IFNγ-inducing therapies such as immune checkpoint blockade can be overcome by intra-tumoral therapeutic delivery of CCL5 resulting in the recruitment of cDC1s. Our findings reveal novel mechanistic insights how to enhance T cell-NK cell-DC crosstalks, enforcing a tumor-eliminating positive feedback mechanism to promote anti-tumor immunity and overcome resistance.

Introduction

Cancer immunotherapy including blockade of immune checkpoints offers great potential to induce durable anti-tumor responses and long-term remission in cancer patients [1–3]. However, multiple mechanisms by which tumors evade immune-mediated rejection have been identified, which result in primary or acquired resistance [4].

The clinical success of immune checkpoint blockade has initially kept the scientific focus predominantly on factors regulating T cell activity and activation [5]. It is, however, increasingly acknowledged that a diverse range of immune cells, including components of innate immunity such as dendritic cells (DCs), must function in a coordinated and synergistic manner to successfully achieve immune-mediated tumor rejection [6–8]. The interferon γ (IFNγ)- Interleukin 12 (IL-12) axis plays a central role in connecting innate and adaptive cancer immunity [9]. Mainly produced by DCs in the tumor microenvironment, IL-12 stimulates cytotoxicity and cytokine-secretion in T cells and natural killer cells (NK cells) [10]. In a positive IL-12-IFNγ feedback loop, T and NK cell-derived IFNγ in turn activates and induces IL-12 expression in DCs. Moreover, IFNγ enhances antigen (cross-)presentation by antigen presenting cells (APCs) and induces secretion of chemokines, thereby further potentiating the cytotoxic activity of CD8 T cells [9,11]. The importance of this immune signaling cascade in cancer is emphasized by the fact that gene expression signatures reflecting cellular components of this axis — NK cells, DCs and CD8 T cells —, and signatures of IFNγ signaling are predictive of improved patient survival and response to immune checkpoint inhibition in multiple cancer types [12–16].

Consequently, IL-12 has been extensively investigated for its use in cancer immunotherapy. When administered systemically, IL-12 has resulted in limited therapeutic benefit but severe dose-limiting toxicity in clinical studies [17,18]. A possible explanation is the lack of targeting to the tumor microenvironment. Most cytokines, including IL-12, act locally in the tumor and nearby lymph nodes in paracrine or autocrine fashion, rather than systemically on lymphocytes in circulation [19]. While multiple approaches using localized IL-12 delivery strategies are currently under investigation to expand the therapeutic window, response to IL-12 alone is rather modest [20–23].

Significant effort is currently directed to introduce combinatorial immunotherapies with the goal to improve therapeutic benefit, either by concomitantly enhancing immune functions or by targeting other immunoregulatory mechanisms within the tumor microenvironment [24–26]. However, despite numerous combination strategies that have been investigated, few have thus far been translated into clinical benefit.

Here, we hypothesize that combining therapeutic strategies that enhance NK cell-DC-T cell crosstalk is essential to strengthen successful anti-tumor responses and to overcome resistance. We show that the described IFNγ-IL-12 axis can be directly utilized and translated into therapeutic approaches by paracrine delivery of IL-12 using a tumor-targeted adenoviral serotype 5 delivery platform as a tool for intra-tumoral immunotherapy (AdV5-IL12) [27–29]. The efficacy of AdV5-IL12 was dependent on the intra-tumoral abundance of NK cells and their ability to prime the immune microenvironment by enhancing DC-CD8 T cell interaction. In tumors with dampened NK cell function, resistance to IL-12 could be rescued by induced expression of CCL5, leading to increased infiltration of cDC1s, which then set the anti-tumor DC-T cell

positive feedback loop in motion. Similarly, resistance to other IFNγ-mediated treatments, such as PD-1 checkpoint blockade, could also be overcome by treatment with CCL5. Our data highlight the importance of the intra-tumoral NK cell-DC-T cell axis for successful cancer immunotherapy. In particular, we show how this crosstalk can be improved by the combination of IFNγ-inducing therapies such as tumor-targeted delivery of IL-12 or anti-PD-1 antibodies with DC attractants such as CCL5.

Results

IL-12 efficacy requires anti-tumor T and NK cell responses

Even though strategies to maximize IL-12 delivery are of increasing clinical interest, the therapeutic benefit in patients remains moderate. We first sought to identify cell types and key pathways underlying successful clinical outcome to intra-tumoral IL-12 therapy in melanoma patients (IL-12MEL trial; NCT01502293) [20]. To this end, we correlated tumor immune signatures derived from pre-treatment tumor biopsies with therapeutic response. Patients with clinical responses showed higher NK cell and CD8 T cell scores compared to patients with tumor progression, while no correlation was found with scores of other immune cells (Figure 1a and Extended data Fig. 1a).

To define a model system for local IL-12 therapy which reflects these clinical findings , we utilized a non-replicative, shielded and re-targeted adenoviral serotype 5 vector previously established in our laboratory [27–29]. For this study, HER2-retargeting was used as a model system to target the HER2-overexpressing syngeneic tumor cell lines B16-HER2 and EMT6-HER2. Due to the high abundance of pre-existing antibodies against AdV5, we made use of a shield based on a hexon-binding humanized single-chain variable fragment (scFv), fully covering the virion [29]. To confirm tumor-specific expression of our payload, luciferase-encoding virus (AdV5-Luciferase) was peritumorally injected into B16-HER2 and EMT6-HER2 bearing mice (Figure Extended data Fig. 1b). In both tumor models, payload was exclusively expressed in the tumor for up to 10 days with a peak expression on day 1 (Extended data Fig. 1 c-e).

To evaluate the efficacy of AdV5 encoding IL-12 (AdV5-IL12), we treated mice bearing orthotopic EMT6-HER2 tumors with four injections of $1.5x10^8$ PFU retargeted and shielded AdV5-IL12 peritumorally. Empty virus (AdV5-control) served as a control (Figure 1b). Treatment with AdV5-IL12 resulted in strong inhibition of tumor growth, enhanced survival and complete tumor regression in 70% of treated mice, while AdV5-control showed only moderate effects. No IL-12 was detected in the serum, confirming the specificity of the tumor-localized therapy (Extended data Fig. 1f). Retargeted and shielded AdV5-IL12 showed increased efficacy compared to naked and retargeted vectors (Extended data Fig. 1g).

AdV5-IL12 induced the formation of a protective anti-tumor immune memory response as mice surviving primary EMT6-HER2 engraftment following AdV5-IL12 treatment remained tumor-free after re-challenge with EMT6-HER2 cells (Extended data Fig. 1h). Tumors from mice simultaneously inoculated with EMT6 wt cells on the lateral flank were equally rejected suggesting broad memory formation against shared antigens expressed in EMT6 cells (Extended data Fig. 1h).

To dissect the role of defined immune cell populations in mediating the therapeutic effect of AdV5-IL12, we performed antibody-mediated depletion studies (Figure 1c). In agreement with the analysis of the immune signatures obtained from the IL-12MEL trial (Figure 1a), AdV5-IL12 required both, CD8 T cells and NK cells, for therapeutic efficacy. In addition, as the clinical response is correlating with a defined IFNγ score [20] and IL-12 is a known driver of IFNγ production in CD8 T cells and NK cells, we assessed the contribution of IFNγ to the activity of AdV5-IL12. IFNγ-neutralizationed mice failed to control EMT6-HER2 tumors upon treatment with AdV5-IL12 (Figure 1d). Thus, mirroring the situation in cancer patients, AdV5-IL12 treatment requires sufficient NK and CD8 T cell response and depends on IFNγ.

As patients with localized IL-12 therapy show clinical responses even in non-treated lesions, we assessed the systemic effect of AdV5-IL12 in our tumor mouse model. To this end, we injected EMT6 wt cells on the contra-lateral side of the EMT6-HER2 tumor (Figure 1e). We observed reduced tumor growth of the contra-lateral tumor and complete regression in 50% of the AdV5-IL12 treated animals (Figure 1f). This indicates potent systemic immune effects upon local administration of AdV5-IL12.

AdV5-IL12 enhances tumor attack by NK and CD8 T cells and stimulates T cell-DC interaction

We next investigated cellular changes in EMT6-HER2 tumors upon treatment with AdV5-IL12 by multiparameter flow cytometry to define changes associated with response to IL-12 (Figure 2a). Consistent to our findings above, AdV5-IL12 primarily induced changes in NK and T cell phenotypes (Figure 2b-c and Extended data Fig. 2). A higher frequency of NK cells in AdV5-IL12 treated tumors compared to the vector control was accompanied by enhanced functionality (CD25+ and PD-1+) and proliferation (Ki67+, Figure 2d and Extended data Fig. 3). Moreover, AdV5-IL12 resulted in a higher frequency of tumor antigen-experienced (CD39+), functional (granzyme B+; GzmB) and proliferating (Ki67+) CD8 T cells (Figure 2e). Durable immunotherapeutic anti-cancer responses require sufficient functionality of CD8 T cells, which can arise from a memory-like CD8 T cell precursor population that expresses Tcf7 and PD-1 ($Tim3^{low}$). This precursor subset, which has characteristics of both progenitor cells and memory cells, can not only give rise to effector cells, but as well to terminally differentiated exhausted T cells ($PD\text{-}1^{hi}$ $Tim3^{hi}$) with limited anti-cancer capacity [30–34]. In tumors treated with AdV5-IL12, the proportion of $PD\text{-}1^{hi}$ $Tim3^{lo}$ was increased whereas the proportion of double-positive CD8 T cells was unchanged (Figure 2f). Ultimately, this resulted in an enhanced proportion of Tcf7+ $PD\text{-}1^{hi}$ $Tim3^{lo}$ precursor subset which has been associated with stem-like properties to promote tumor control [30–34].

Next, we assessed the capability of NK and CD8 T cells to directly interact and attack cancer cells using a highly multiplexed cytometric imaging approach, termed co-detection by indexing (CODEX) [35]. AdV5-IL12 led to pronounced accumulation of CD45+ immune cells (Extended data Fig. 4a-b). Spatial proximity (defined as a distance of <50 µm) of NK and CD8 T cells with tumor cells was specifically increased upon AdV5-IL12 treatment (Figure 2g and Extended data Fig. 4c). To confirm biological interactions and tumor lysis by NK and CD8 T cells, we analyzed the expression of the effector marker granzyme B in cells with spatial proximity to tumor cells (CD45- CD31-). In both NK and CD8 T cells, the number of granzyme B+ cells was increased in close proximity to tumor cells (Figure 2h). In addition, spatial proximity of CD8 T cells with DCs was specifically enhanced after AdV5-IL12 treatment (Figure 2g). Futhermore, the co-stimulatory molecules, CD40, CD80 and MHCII, as well as PD-L1 on DCs in close proximity to CD8 T cells were specifically increased after AdV5-IL12 treatment, indicating an enhanced functional interaction between DCs and CD8 T cells induced by IL-12 (Figure 2i).

CCL5 induction by NK cells determines IL-12 response

We also noticed close proximity of CD8 and NK to endothelial cells after AdV5-IL12 treatment (Figure 2g and j). To investigate potential recruitment of these cells to the tumor, we blocked lymphocyte recirculation

with the trafficking inhibitor FTY720 [36]. FTY720 treatment prior to tumor inoculation fully abrogated tumor control, while blocking trafficking during AdV5-IL12 treatment allowed initial tumor control, but did not result in complete tumor regression (Figure 3a). This suggests that efficient IL-12 response requires both pre-existing and actively recruited tumor infiltrating lymphocytes.

In addition to direct cytotoxicity against tumor cells, NK cells were shown to drive immune cell infiltration and intrinsic inflammation within tumors [6,13]. To better understand such a potential dual role of NK cells, we depleted NK cells throughout the AdV5-IL12 treatment and assessed fate and infiltration of tumor-infiltrating immune cells (Figure 3b and Extended data Fig. 3). NK cell depletion led to a reduced number of MHCII+ CD103+ conventional dendritic cells (cDC1s, CD11c+ F4/80-; Figure 3c). Furthermore, NK depletion was associated with reduced granzyme B expression in CD8 T cells, suggesting an important role of NK cells in facilitating optimal anti-tumor CD8 T cells responses (Figure 3d). While the number of macrophages (CD11b+ F4/80+) in the tumor was unchanged, depletion of NK cells skewed the polarization towards an immunosuppressive M2 (CD206+ MHCII-) phenotype (Figure 3e). Thus, we concluded that during AdV5-IL12 treatment, NK cells orchestrate the recruitment and priming of other cell subsets including cDC1s and activated CD8 T cells to enhance tumor killing.

To identify clinically relevant chemokines which may guide immune cell recruitment by NK cells after IL-12 therapy, we correlated NK cell scores with the expression of chemokines and their receptors in patients responding to IL-12 therapy (Figure 3f). We identified CCL5 and its receptor CCR5 which strongly correlated with the NK score (Figure 3g). Accordingly, CCL5 was significantly upregulated in patients with clinical response (Figure 3h). These results indicate that NK cells and the CCL5 axis are important in facilitating clinical responses to IL-12.

Next, we investigated whether NK cell-mediated CCL5 contributes to efficacy of AdV5-IL12 in EMT6-HER2 tumors. We first showed that CCL5 concentration was dramatically reduced in tumor lysates after NK cell depletion, which confirms NK cells as the main source of CCL5 in this model (Figure 3i). Mirroring the CLL5 upregulation in responding patients (Figure 3h), AdV5-IL12 treatment of EMT6-HER2 tumors induced CCL5 production in NK cells. Neutralizing CCL5 using antibodies starting one day before tumor inoculation fully abrogated IL-12 efficacy, while CCL5 neutralization starting one day before AdV5-IL12 treatment partially inhibited efficacy (Figure 3j). Therefore, we concluded that CCL5 produced by NK cells plays a dual role in the efficacy of IL-12. While CCL5 at steady state permits responsiveness to AdV5-IL12 treatment, further induction of CCL5 by AdV5-IL12 treatment may attract immune cells to improve anti-tumor immunity.

AdV5-CCL5 rescues AdV5-IL12 resistance in tumor models with dampened NK cell function

To analyze the contribution of CCL5 to NK cell-mediated tumor rejection upon AdV5-IL12 treatment, NK-depleted tumor-bearing mice were concomitantly treated with IL-12 and CCL5, both using our adenoviral platform (AdV5-IL12 + AdV5-CCL5; Figure 4a). While depletion of NK cells abrogated the efficacy of AdV5-

IL12 (Fig 1c), the combination of AdV5-CCL5 with AdV5-IL12 partly rescued the efficacy, resulting in improved but not complete tumor rejections. AdV-CCL5 alone did not have any effect (Figure 4b).

Consequently, we asked whether AdV5-CCL5 can further boost AdV5-IL12 efficacy in tumor models with dampened anti-tumor NK cell function. Unlike in EMT6-HER2, NK cell depletion in B16-HER2, a well-known aggressive and immune-excluded tumor model, did not increase tumor growth in neither untreated nor AdV5-IL12 treated tumors (Figure 1c and 4c). Similarly, as NK cells are driving immune cell infiltration in AdV5-IL12 treated EMT6-HER2 tumors (Figure 3a), AdV5-IL12 response in B16-HER2 tumors was not affected by FTY720, suggesting that trafficking of immune cells does not contribute to therapeutic efficacy in this model (Figure 4d). Additionally, the low impact of NK cell depletion in B16-HER2 tumors was accompanied by lower levels of CCL5 (Figure 4e).

We next asked if AdV5-CCL5 can compensate reduced NK cell-derived CCL5 when combined with AdV5-IL12 in B16-HER2 bearing mice (Figure 4f**).** Indeed, the combination further delayed tumor growth and increased survival compared to single treatments (Figure 4g). Taken together, these data suggest that in tumor models with low CCL5 levels, presumably as a result of dampened NK cell function, IL-12 responses can be boosted by intra-tumoral delivery of CCL5.

To show the potential of our adenoviral vector as a platform for combinatorial approaches, we then designed adenoviral vectors expressing both, IL-12 and CCL5 (Extended data Fig. 5a). To avoid gene deletion of IL-12 or CCL5 from the adenoviral vectors by homologous recombination, we encoded both transgenes under the control of the orthogonal promotors, CMV or SV40. We were able to demonstrate similar therapeutic efficacy by expressing both payloads within one viral vector, independent of the choice of promotor, despite the fact that we thereby decreased the total viral load per injection (Extended data Fig. 5b-c).

AdV5-CCL5 improves IL-12 response by inducing DC-CD8 T cell crosstalk

To mechanistically understand the contribution of AdV5-CCL5, we first investigated the role of CCL5-mediated lymphocyte trafficking in mediating therapeutic efficacy of the AdV5-CCL5/AdV5-IL12 combination (Figure 5a). FTY720 treatment diminished the benefit of the combination compared to AdV5-IL12 single treatment, suggesting that CCL5 predominantly acts by mechanisms depending on cell migration (Figure 5b).

To define factors which could explain the lack of efficacy of IL-12 in the $CCL5^{low}$ compared to the $CCL5^{high}$ model, we compared induced cell interactions after IL-12 therapy in B16-HER2 versus EMT6-HER2 tumors (Figure 5c and Extended data Fig. 6). We observed two major differences in the induced interactome in treated B16-HER2 tumors: a) less induction of NK cell-tumor cell and CD8 T cell-tumor cell interactions, and b) lower induction of DC-CD8 T cell interactions in the $CCL5^{low}$ tumor microenvironment. This suggests a reduced tumor attack of effector cells, as well as a reduced induction of DC-CD8 T cell crosstalk by IL-12 in $CCL5^{low}$ tumors.

To further decipher the intra-tumoral cellular mechanisms, we performed multiparameter flow cytometry analysis after treatment with AdV5-IL12 alone and in combination with AdV5-CCL5 in the $CCL5^{low}$ tumor

model (Figure Extended data Fig. 3). We could show that AdV5-IL12 increased the CD8/Treg ratio, which is associated with improved anti-tumor responses (Figure 5d) [37]. This effect could not be further increased when combining AdV5-IL12 with AdV5-CCL5 (Figure 5d). Similarly, the AdV5-CCL5/AdV5-IL12 combination enhanced the expression of granzyme B in both CD8 T cells and NK cells, compared to untreated tumors, with no significant increase compared to AdV5-IL12 (Figure 5e).

CCL5 produced by NK cells has been shown to induce cDC1 recruitment into the tumor [13]. Accordingly, we were able to detect increased numbers of cDC1s in the tumor after AdV5-CCL5 treatment, either alone or in combination with AdV5-IL12, and, importantly, unlike single AdV5-IL12 treatment (Figure 5f). We also found an increased number of cDC1s expressing CD80 and PD-L1 exclusively in response to the AdV5-CCL5/AdV5-IL12 combination, suggesting enhanced activation through increased IFNγ levels (Figure 5g).

Next, we assessed whether therapeutic CCL5 supplementation can rescue the lack of CD8 T cell-DC crosstalk in the $CCL5^{low}$ tumor. Indeed, CCL5 led to a higher amount of interactions between DCs and CD8 T cells (Figure 5h). The latter was accompanied by a higher expression of effector molecules on CD8 T cells in close contact to DCs (Figure 5i). In addition, we could observe an increased number of interactions between DCs and tumor cells (Extended data Fig. 6c). To further understand the contribution of DCs to the therapeutic efficacy of the AdV5-IL12-AdV5-CCL5 combination we used Batf3 KO mice, which lack cDC1s [38]. Strikingly, the beneficial effect of AdV5-IL12 +/- AdV5-CCL5 on tumor control and survival were lost in Batf3 KO mice (Figure 5j). Taken together, these data suggest that cDC1s attracted by CCL5 are essential for IL-12-mediated therapeutic benefit by enhancing T cell-mediated immunity.

AdV5-huIL-12 induces CCL5 expression in patient-derived tumor cultures

To test whether a human IL-12-encoding HER2-targeted and shielded adenoviral vector (AdV5-huIL12) can induce similar anti-tumorigenic effects in a human *ex vivo* system, we co-cultured primary tumor suspensions containing tumor infiltrating lymphocytes (TILs) from non-small cell lung cancer patients (Figure 6a) or peripheral blood mononuclear cells of healthy donors (HD PBMCs, Figure Extended data Fig. 7) with a HER2-expressing ovarian cancer cell line (OVCAR3), which was transduced with human IL-12-encoding adenoviral vector (Figure 6a-e). This experimental system has been shown to activate primary human lymphocyte subsets and trigger human cancer cell killing in response to PD-1/PD-L1 blockade [39]. Within patient-derived TILs and OVCAR3 co-cultures, AdV5-huIL12 significantly reduced OVCAR3 viability due to enhanced tumor cell killing (Figure 6b). This was similarly achieved when PBMCs were co-cultured with OVCAR3 (Extended data Fig. 7a). This effect was accompanied by an increase in IFNγ secretion (Figure 6c and Extended data Fig. 7b) and induction of IFNγ-expressing patient-derived or healthy-donor CD8 T cells and NK cells (Figure 6d, Extended data Fig. 7c, respectively). In line with our murine data, CCL5 was upregulated by IL-12, an effect that was NK cell-dependent (Figure 6e and Extended data Fig. 7d).

Next, we assessed the activity of AdV5-huIL12 using a patient-derived tumor fragment platform, a human *ex vivo* model that preserves the tumor microenvironment and architecture, but enables *ex vivo* perturbation by checkpoint blockade (Figure 6f) [40]. Tumor fragments of HER2-expressing ovarian cancer

samples were embedded in Matrigel (Figure 6g) and transduced with HER2-retargeted human IL-12-encoding adenoviral vector. In all four tested patients, we could see an upregulation of IFNγ in CD8 T cells, as well as upregulation of CCL5 in NK cells (Figure 6h). The latter was confirmed in the supernatant by ELISA (Figure 6i).

Collectively, these experiments with primary human tumors recapitulate our observations in mice that IL-12 can directly stimulate tumor-infiltrating T cell antitumor activity and induce CCL5 upregulation by NK cells.

CCL5 expression is beneficial for anti-PD-1 efficacy

It has been demonstrated that IL-12-producing DCs, activated by IFNγ-secreting CD8 T cells, are critical for successful responses to anti-PD-1 treatments [9]. This led us to investigate whether the DC attractant CCL5 is associated with efficient tumor responses to anti-PD-1 therapy.

In melanoma patients undergoing nivolumab treatment [41], we compared CCL5-induction during treatment between responding (R) and non-responding (NR) patients (Figure 7a). Indeed, CCL5 upregulation was significantly associated with response in the tested cohort (Figure 7b). Using an NK cell signature as a surrogate of NK cell abundance, we observed a positive correlation between the NK signature and CCL5 expression, consistent with intra-tumoral NK cells in patients being a source of CCL5 (Figure 7c) [13]. Furthermore, using gene signatures for cDC1s to estimate cellular abundance, we also found a positive correlation between levels of CCL5 and cDC1s in treated melanoma patients (Figure 7d), which is in alignement with the observed cDC1 recruitment by CCL5 in our tumor model (Figure 5f).

Utilizing the patient-derived tumor fragment platform, we recently demonstrated that the clinical response of patients to PD-1 blockade correlates with the capacity of intra-tumoral immune cells to be reactivated by anti-PD-1 *ex vivo* [40]. We therefore measured IFNγ and CCL5 in the supernatants of tumor fragments from cancer patients and exposed them to anti-PD-1 (Figure 7e). In line with the clinical data (Figure 7b), we found an upregulation of CCL5 in responding fragments (IFNγ upregulation) after anti-PD-1 blockade (Figure 7g).

Consequently, we asked whether CCL5 can further boost anti-PD-1 therapy in our tumor model with low endogenous CCL5 level. We combined anti-PD-1 therapy with our adenoviral vector encoding CCL5 in B16-HER2 bearing mice (Figure 7h). While AdV5-CCL5 single treatment did not show any therapeutic efficacy, we observed synergistic therapeutic effects when combined with anti-PD-1 treatment.

Taken together, these data demonstrate that CCL5 exerts promising therapeutic potential through recruitment of cDC1s. Thus, the IL-12-IFNγ-CCL5 axis represents a tangible target to improve PD-1 checkpoint blockade therapy.

Discussion

Combination immunotherapies have become a cornerstone in the therapeutic management of patients with different cancer types and are being extensively explored to overcome resistance to cancer immunotherapies such as checkpoint blockade and IL-12 therapy [42–45]. Here, we identify a novel mechanism-driven combinatorial approach which improves therapeutic outcomes of targeted IL-12 and anti-PD-1 treatment by exploiting key cellular components and processes in the tumor microenvironment. We show that IL-12 enhanced anti-tumorigenic DC-CD8 T cell interactions which relied on NK cell-specific induction of CCL5. Consequently, in tumor models with dampened NK function and thus low CCL5 levels, only moderate IL-12 responses were observed. However, responses of NK cell-dampened tumors could be rescued by concomitant administration of a CCL5-encoding adenoviral vector which - after converting tumor cells into CCL5 production sites - induced cDC1 infiltration and thus increased DC-CD8 T cell interactions (Extended data Fig. 8). Due to the unique role of cDC1s in the initiation of T cell responses, both *de novo* and upon anti-PD-1 checkpoint inhibition, we subsequently observed synergistic efficacy of AdV5-CCL5 and anti-PD-1 treatment. These findings allow to improve immunotherapy by fine-tuning the crosstalk between lymphoid and myeloid immune compartments. This offers opportunities for rational drug combinations adjusted to the pre-existing tumor microenvironment.

Viral vectors have been shown to be a suitable tool for local immunotherapy, reducing the systemic spread of therapeutic agents and consequently avoiding systemic side effects [46]. Our adenoviral platform utilizes exogenously added retargeting adaptors consisting of DARPins [47]. This strategy has unique advantages, compared to targeting by genetic modifications, including the large existing library of DARPins and the rapid selection of new DARPin adapters against any given surface protein [48,49]. Here, we targeted the model tumor-antigen HER2 which is overexpressed in different cancer types [50]. To further broaden the clinical applicability, DARPins may be selected to specifically recognize targets on cells other than tumor cells, such as fibroblast activation protein (FAP) on tumor-associated fibroblasts [51,52]. Recently, the development of high-capacity, helper-dependent AdVs has enabled the expression of transgenes of up to 36 kilobase pairs. This, in combination with the targeted and shielded strategy, has increased the potential of AdVs as an ideal vector for combinatorial cancer immunotherapy [29,53]. Previous work has shown that adenoviral vectors can act as a "self-adjuvants", allowing the stimulation of multiple innate immune signaling pathways such as toll-like receptors and the induction of type I interferons upon viral entry [54–56]. While these effects may explain the effect of the empty AdV5-control in tumor delay, the improved anti-tumor immunity supports the potential advantage of adenoviral vectors compared to other gene delivery vectors [57,58].

The efficacy of immunotherapy is dependent on a variety of factors and cell types in the tumor microenvironment, and untangling these complex interactions is critical to understand and improve therapeutic efficacy. Dendritic cells play a key role in orchestrating anti-tumor immunity. Although typically rare, they include distinct subsets with non-overlapping functions that can be harnessed for cancer immunotherapy [59]. Intra-tumoral presence of DCs and their production of IL-12 has been associated with better survival in various cancer types and is positively correlated with clinical outcome to anti-PD-1 therapy

[6]. Consequently, IL-12 has been extensively investigated for use in cancer immunotherapy. However, many previous attempts to develop IL-12-based therapies for use in humans resulted in severe toxicities and limited response rates even in tumor-targeted approaches [18,60]. Utilizing the AdV5 platform, our data demonstrate the potential of IL-12 to bridge innate and adaptive immunity for successful development of anti-tumor immunity. IL-12 produced by tumor cells after treatment with AdV5-IL12 increased activation and cytotoxic potential of murine and human CD8 T cells. Although we could show that early tumor growth control is achieved by the steady state of lymphocytes present within the tumor, our results suggest that lymphocyte- and antigen-trafficking to draining lymph nodes is needed for long-term tumor rejection. In agreement, we observed increased numbers of NK cells and CD8 T cells in close proximity to blood vessels which may indicate an enhanced trafficking from the periphery to the tumor. This may be induced by the observed CCL5 secretion by NK cells or other IFNγ-induced chemokines such as CXCL9 and CXCL10. The fact that cDC1s have been described as the main source of CXCL9 and CXCL10 [61] could explain the increased interactions between DCs and CD8 T cells and therefore increased T cell immunity after AdV5-IL12 treatment. Consequently, we demonstrated that AdV5-IL12 not only improves lymphocyte homing and activation in the primary tumor, but also promotes abscopal anti-tumor effects at distant tumor sides.

NK cells contribute to various immune functions during cancer initiation and progression, including the recognition of cells undergoing stress or early transformation and the direct killing of sensitive cells [8]. In addition to rapid degranulation upon target recognition, NK cells are powerful producers of a broad variety of pro-inflammatory cytokines and chemokines shaping the inflammatory milieu of tumors [6,13]. Several preclinical models have confirmed that NK cells are required for optimal anti-tumor CD8 T cell responses by recruiting cDC1s and subsequently CD8 T cells [8]. Consistent with these models, there is growing evidence that the magnitude of NK cell infiltration has a strong prognostic value in various cancers, and predicts clinical outcome to immune checkpoint blockade in different tumor types [62]. In our study, NK cells and their expression of CCL5 were essential for the efficacy of AdV5-IL12 and were correlating with response to anti-PD-1 and IL-12 therapy in human melanoma. These data confirm the crucial role of NK cells in priming the tumor immune microenvironment by inducing DC-CD8 T cell interactions and provide direct evidence that lack of intra-tumoral cDC1 recruitment by NK cells represents a major barrier of T cell-based therapies. However, further work will need to identify tumor-derived factors that mediate resistance by limiting accumulation, survival, and function of these cells within the tumor microenvironment. Such factors may serve as predictive markers for T cell-focused therapies and define the need for potential combinations with cDC1 attracting agents. With regard to the latter, we here identify CCL5, which we show to improve the efficacy of IFNγ-inducing therapies, such as IL-12 or checkpoint inhibition in tumors with dampened NK function.

Some controversy exists regarding the role of CCL5 in cancer. A number of studies suggest CCL5 to have potential tumor-promoting effects, either by directly affecting tumor growth [63], fostering an immunosuppressive tumor microenvironment [64], enhancing tumor cell migration [65], or expanding cancer stem cells [66]. In contrast, other studies show delayed tumor growth and prolonged survival in mouse models with CCL5-expressing tumor cells, as well as correlation between CCL5 expression and a T cell-

inflamed phenotype in cancer patients [67–69]. In our models, AdV5-CCL5 did not exhibit any tumor-promoting effects, but also failed to show therapeutic benefits as a monotherapy. Notably, in agreement with previous work [13], AdV5-CCL5 treatment induced cDC1 recruitment. However, only the combination with AdV5-IL12, led to higher co-stimulatory potential and subsequently increased tumor-reactive T cells. This suggests that the anti-tumorigenic properties of CCL5 are likely context-dependent: in the presence of other anti-tumorigenic signals induced by IL-12 or anti-PD1 treatment - which are known to tip the balance to a pro-inflammatory environment - CCL5 may further boost these effects which then translates into improved responses as evidenced by our *in vivo* data and analysis of patient cohorts. Besides CCL5, XCL1 has been described to have similar capacities in recruiting cDC1s to the tumor bed while not being reported to have tumor-promoting capacities [13]. On this note, XCL1 might be an intuitive alternative payload to guide cDC1s into tumors to improve anti-tumor immunity.

Taken together, our data highlight the importance of NK cells and their capability to induce T cell immunity by enhancing DC-T cell crosstalk in IFNγ inducing therapies and may inform novel combination strategies utilizing viral vector platforms as an approach to further potentiate this NK cell-DC-T cell crosstalk. Our data highlight a relevant tumor-eliminating positive feedback mechanism to be prioritized for clinical development, particularly in patients with immune-excluded and/or resistant tumors.

Figures

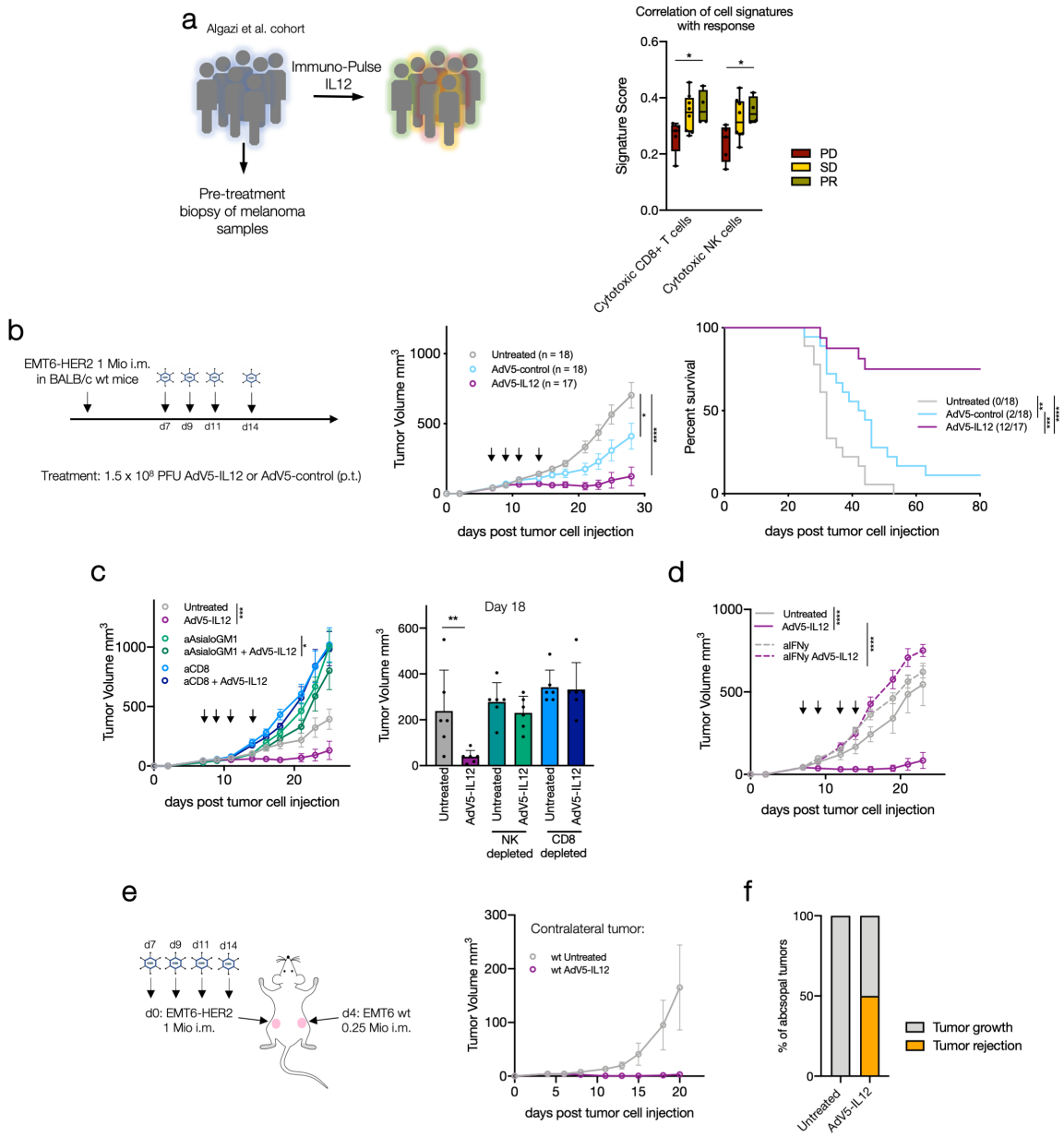

Figure 1: IL-12 efficacy requires anti-tumor T and NK cell responses

a: Cell signature scores measured by Nanostring in skin tumor biopsies from 19 melanoma patients before intra-tumoral treatment with ImmunoPulse IL-12 were correlated with clinical response (PD: progressive disease, SD: stable disease, PR: partial response) [20]. **b:** Wildtype (WT) mice were engrafted with 1 mio EMT6-HER2 intramammarily (i.m.). From day 7 (tumor size 30–70 mm^3), mice were treated with $1.5x10^8$ PFU of HER2-targeted and shielded adenoviral vectors (peritumorally, p.t.) encoding for IL-12 or an empty control cassette (AdV5-control) on days 7, 9, 11 and 14 p.t. Tumor growth and Kaplan-Meier survival curves are shown with the number of mice indicated. Black arrows denote days of treatment. **c-d:** For depletion and neutralization studies, mice were injected i.p. with anti-CD8, anti-AsialoGM1 or anti-IFNγ, starting one day before adenoviral treatment. Tumor growth curves after depletion or neutralization are shown. Black arrows denote days of adenoviral treatment. n = 6 mice. **e-f:** Wildtype (WT) mice were

engrafted with 1 mio EMT6-HER2 (i.m.) and with 4 days delay with 0.25 mio EMT6 wt cells on the contralateral flank. EMT6-HER2 tumors were peritumorally treated with AdV5-IL12. Tumor growth of contralateral tumor (EMT6 wt) was measured. Tumor growth curve and percentage of rejected contralateral tumors are shown. n = 6 mice per group.

*p < 0.05, **p < 0.01, ***p < 0.001, ****p < 0.0001. Error bar values represent SD or SEM (tumor growth curves). For comparisons between three or more groups, one-way ANOVA with multiple comparisons was used. For survival analysis, p values were computed using the Log Rank test. Two-way ANOVA was used to compare tumor growth curves. See also Extended data Fig. 1.

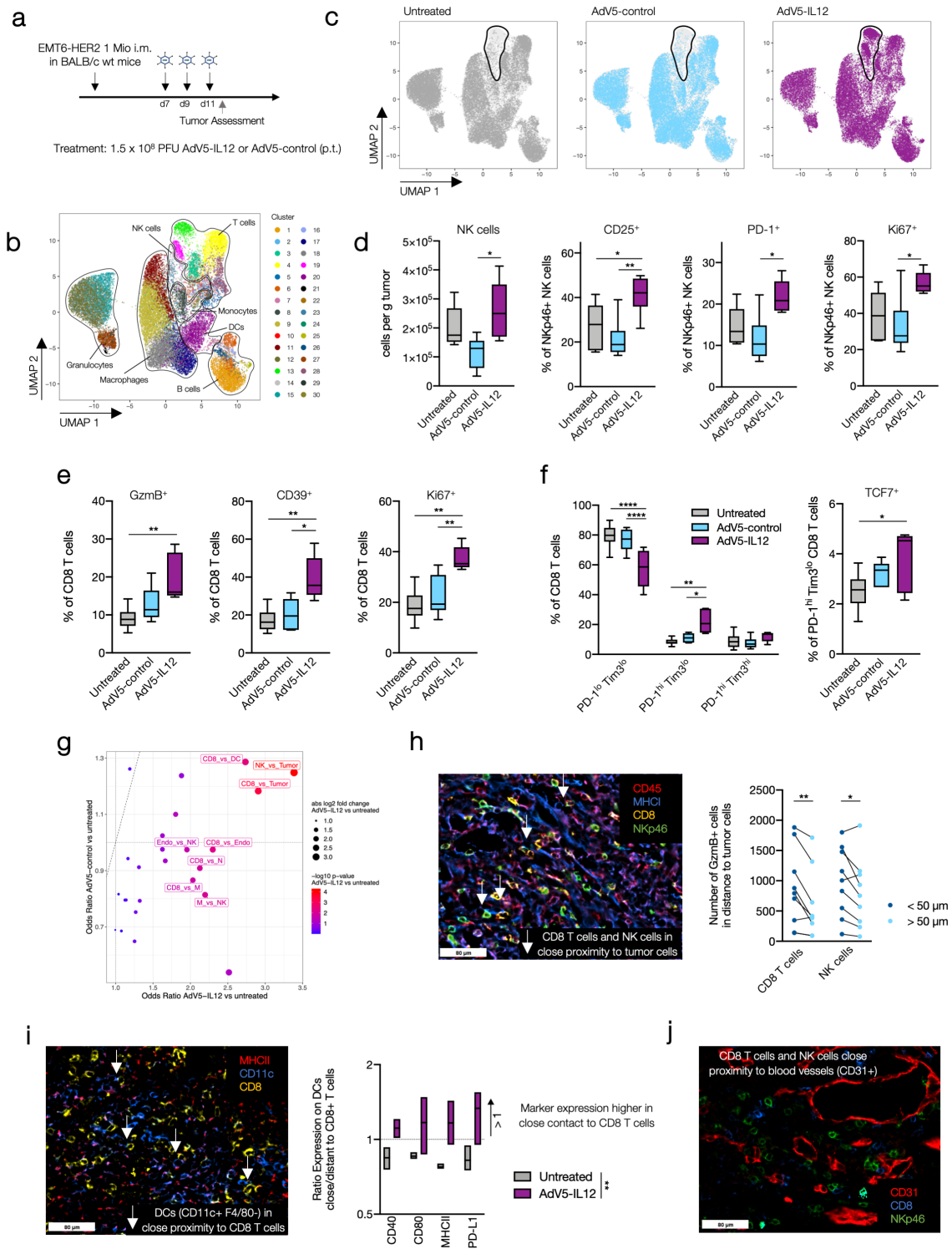

Figure 2: AdV5-IL12 enhances tumor attack by NK and CD8 T cells and stimulates T cell-DC interaction

a-f: Wildtype (WT) mice were engrafted with 1 mio EMT6-HER2 intramammarily (i.m.). Starting from day 7 (tumor size 30–70 mm^3), mice were treated with 1.5x10^8 PFU of HER2-targeted and shielded adenoviral vectors (p.t.) encoding for IL-12 or empty control cassette (AdV5-control) on day 7, 9 and 11. On day 12 post inoculation, tumors were isolated and single cell suspensions were analyzed by flow cytometry. **b:** UMAP projection is depicting the alive CD45+ tumor infiltrating lymphocytes colored by cluster. **c:** UMAP

projection is showing distribution of cells colored by treatment condition (dark grey: untreated; blue: AdV5-control; magenta: AdV5-IL12). **d:** Quantification of NK cells (NKp46+, CD3-, Ly6G-, CD19-, F4/80-) per gram tumor and proportion of CD25+, PD-1+ or Ki67+ of NK cells between the different treatment conditions. **e-f:** Proportion of granzyme B+ (GzmB+), CD39+ or Ki67+ of CD8 T cells (CD3+, CD4-, NKp46-, CD19-) between the different treatment conditions. Proportion of PD-1^{lo}TIM3^{lo}, PD-1^{hi}TIM3^{lo} or PD-1^{hi}TIM3^{hi} intra-tumoral CD8 T cells in each treatment group. **a-f:** n = 5-6 mice per group. *p < 0.05, **p < 0.01, ***p < 0.001, ****p < 0.0001. Error bar values represent SD. For comparisons between three or more groups, one-way ANOVA with multiple comparisons was used. **g-j:** Wildtype (WT) mice were engrafted with 1 mio EMT6-HER2 (i.m.). Starting from day 7 (tumor size 30–70 mm^3), mice were treated with 1.5x10^8 PFU of HER2-targeted and shielded adenoviral vectors (p.t.) encoding for IL-12 or empty control cassette (AdV5-control) on day 7, 9 and 11. On day 12 post inoculation, tumors were isolated, embedded in OCT and analyzed by multiparameter immuno-fluorescence microscopy. **g:** Visualization of odds ratios and p values for changes in cell-cell type interactions between experimental conditions focusing on interaction including CD8 T cells and NK cells. **h:** Representative IF pictures are showing AdV5-IL12 treated tumors (CD45: red, MHCI: blue, CD8: yellow, NKp46: green). White arrows are showing CD8 T cells (CD45+, MHCI+, CD8+) or NK cells (CD45+, MHCI+, NKp46+) neighboring tumor cells (CD45-, MHCI+). Quantification of GzmB+ CD8 T cells and NK cells in close proximity (<50 µm) to tumor cells in comparison to more distant (>50 µm) proximity. Each dot represents the count in one acquired tumor. Treatment conditions were pooled in this analysis. **i:** Representative IF pictures are showing AdV5-IL12 treated tumors (MHCII: red, CD11c: blue, CD8: yellow). White arrows are showing CD8 T cells (CD45+, CD8+) neighboring DCs (CD45+, CD11c+, F4/80-). Ratio of CD40, CD80, MHCII and PD-L1 expression on the DC cluster in close (<50 µm) or distant (>50 µm) proximity to CD8 T cell cluster comparing untreated and AdV5-IL12 treated tumors. **j:** Representative IF pictures showing CD8 T cells and NK cells in close proximity to blood vessels in AdV5-IL12 treated tumors (CD31: red, CD8: blue, NKp46: green). **g-j:** n = 3 mice per group. *p < 0.05, **p < 0.01, ***p < 0.001, ****p < 0.0001. For comparisons between three or more groups, one-way ANOVA with multiple comparisons was used. See also Figure Extended data Fig. 2, 3 and 4.

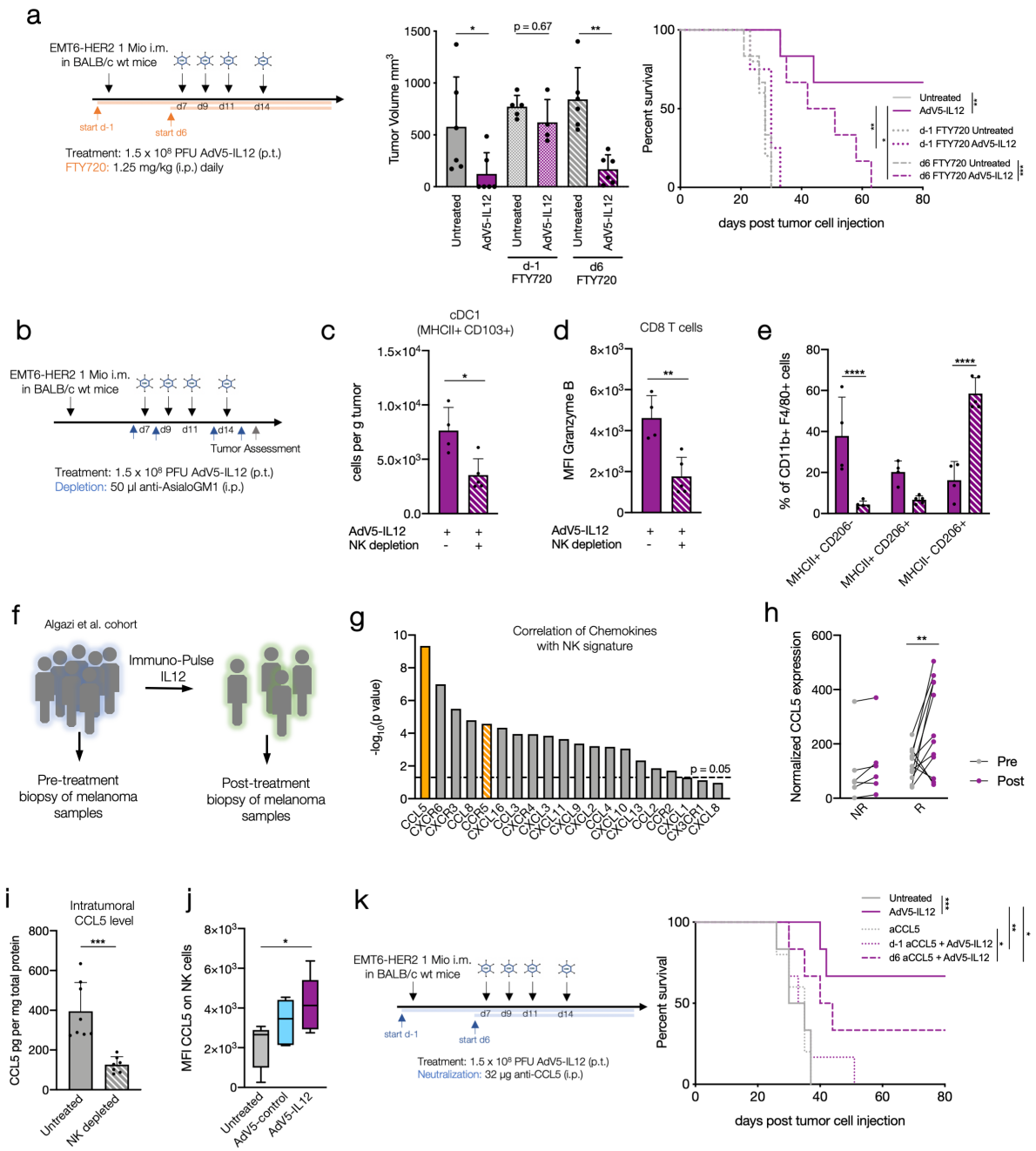

Figure 3: CCL5 induction by NK cells determines IL-12 response

a: 1 mio EMT6-HER2 cells were injected in WT mice (i.m.). Starting from day 7 (tumor size 30–70 mm^3), mice were treated with $1.5x10^8$ PFU of HER2-targeted and shielded adenoviral vectors (peritumorally) encoding for IL-12 on day 7, 9, 11 and 14. Lymphocyte trafficking was inhibited using FTY720 as indicated (orange arrow and line). Tumor volume on day 23 post tumor inoculation and Kaplan-Meier survival curves are shown. **b-e:** 1 mio EMT6-HER2 cells were injected in WT mice (i.m.). Starting from day 7 (tumor size 30–70 mm^3), mice were treated with $1.5x10^8$ PFU of HER2-targeted and shielded adenoviral vectors (p.t.) encoding for IL-12 on day 7, 9, 11 and 14. NK cells were depleted using 50 µl anti-AsialoGM1 antibody (i.p) as indicated (blue arrow). Tumors were isolated and single cell suspensions of tumors digest were analyzed using flow cytometry on day 16. **c:** Intra-tumoral cDC1s (CD11c+, F4/80-, Ly-6G-, MHCII+, CD103+, CD11blow) were quantified after AdV5-IL12 treatment +/- NK depletion. **d:** Mean fluorescence

intensity (MFI) of granzyme B on CD8 T cells (CD3+, CD8+, NKp46-, CD19-, Ly-6G-). **e:** Polarization of macrophages (CD11b+ F4/80+) after AdV5-IL12 treatment comparing NK depletion versus non-depleted. **a-e:** n = 4-5 mice per group. *p < 0.05, **p < 0.01, ***p < 0.001, ****p < 0.0001. Error bar values represent SD. 2-tailed Student's t tests were used. For comparisons between grouped data sets, two-way ANOVA with multiple comparisons was used. **f-g:** -log10(p value) of chemokines and their receptors which are correlating with NK signature of skin tumor biopsies from melanoma patients responding to intra-tumoral treatment with ImmunoPulse IL-12 are shown. **h:** Normalized CCL5 expression of patients with no-response (NR: PD) versus response (R: SD + PR) before and after intra-tumoral treatment with ImmunoPulse IL-12. **f-h:** *p < 0.05, **p < 0.01, ***p < 0.001, ****p < 0.0001. Error bar values represent SD. **i-j:** Wildtype (WT) mice were engrafted with 1 mio EMT6-HER2 (i.m.). **h:** NK cells were depleted using 50 µl anti-AsialoGM1 antibody (i.p) every 3-4 days. On day 7 post inoculation (tumor size 30–70 mm^3), tumors were isolated and lysed. CCL5 expression was determined by ELISA and normalized to total protein measured by BCA. n= 6 per condition. 2-tailed Student's t test was used. **i:** Starting from day 7 (tumor size 30–70 mm^3), mice were treated with $1.5x10^8$ PFU of HER2-targeted and shielded adenoviral vectors (p.t.) encoding for IL-12 or empty control cassette (AdV5-control) on day 7, 9 and 11. On day 12 tumors were isolated and CCL5 expression (MFI) was analyzed on NK cells. n= 6 mice per condition. One-way ANOVA with multiple comparisons was used. **k:** Wildtype (WT) mice were engrafted with 1 mio EMT6-HER2 (i.m.). Mice were treated with AdV5-IL12 following the indicated schedule. Starting one day prior tumor inoculation or one day prior adenoviral therapy, CCL5 was neutralized using antibodies every 3-4 days. Tumor growth and Kaplan-Meier survival curves are shown. Black arrows denote days of treatment. *p < 0.05, **p < 0.01, ***p < 0.001, ****p < 0.0001. Error bar values represent SEM. For survival analysis, p values were computed using the Log Rank test. Two-way ANOVA was used to compare tumor growth curves. See also Figure Extended data Fig. 3.

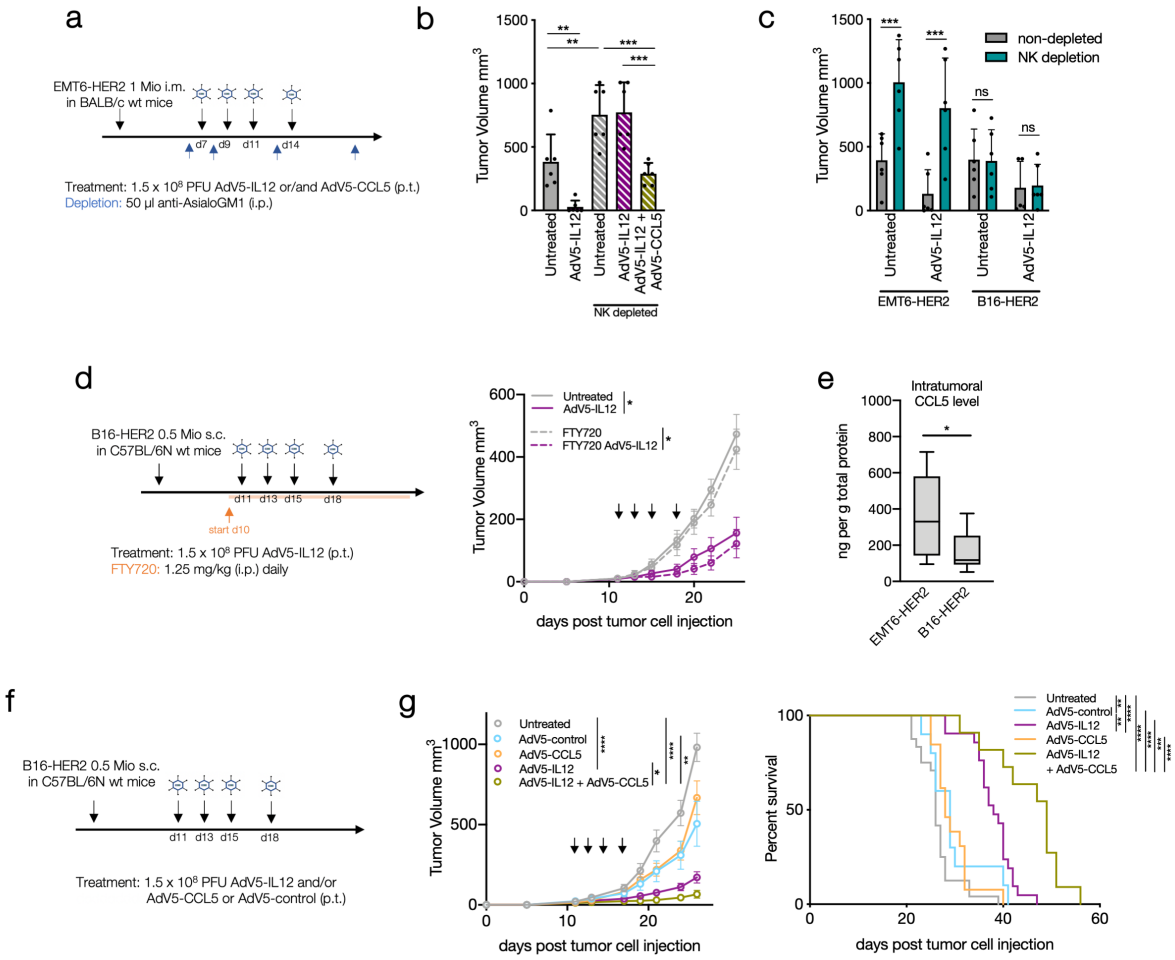

Figure 4: AdV5-CCL5 rescues AdV5-IL12 resistance in tumor models with dampened NK cell function

a: Wildtype (WT) mice were engrafted with 1 mio EMT6-HER2 (i.m.). Mice were treated with AdV5-IL12 and AdV5-CCL5 following the indicated schedule. Starting one day prior adenoviral therapy, NK cells were depleted using anti-AsialoGM1 antibody as indicated (blue arrow). **b:** Tumor volume on day 23 post tumor inoculation is shown. **c:** Wildtype (WT) mice were engrafted with 1 mio EMT6-HER2 (i.m.) or 0.5 mio B16-HER2 (s.c.). Mice were treated with AdV5-IL12 on day 7, 9, 11 and 14 or day 11, 13, 15 and 18 (tumor size 30–70 mm^3), respectively. NK cells were depleted using anti-AsialoGM1 and anti-NK1.1 antibody every 4-5 days starting one day prior adenoviral therapy. Tumor volume on day 25 post tumor inoculation is shown. **d:** Wildtype (WT) mice were engrafted with 0.5 mio B16-HER2 (s.c.). Mice were treated with AdV5-IL12 on day 11, 13, 15 and 18 (tumor size 30–70 mm^3). Lymphocyte trafficking was inhibited using FTY720 as indicated (orange arrow and line). Tumor growth curves are shown. **e:** Intra-tumoral CCL5 concentration was determined by ELISA and normalized to total protein in EMT6-HER2 and B16-HER2 tumor lysates. **f-g:** Mice were treated with AdV5-IL12 and AdV5-CCL5 on day 11, 13, 15 and 18 (tumor size 30–70 mm^3) after B16-HER2 inoculation as indicated**:** Tumor growth and Kaplan-Meier survival curves are shown (n > 15 mice per condition). **a-g:** n = at least 6 mice per group. *p < 0.05, **p < 0.01, ***p <

0.001, ****p < 0.0001. Error bar values represent SD or SEM (tumor growth curves). For comparisons between three or more groups, one-way ANOVA with multiple comparisons was used. For survival analysis, p values were computed using the Log Rank test. Two-way ANOVA was used to compare tumor growth curves. See also Figure Extended data Fig. 5.

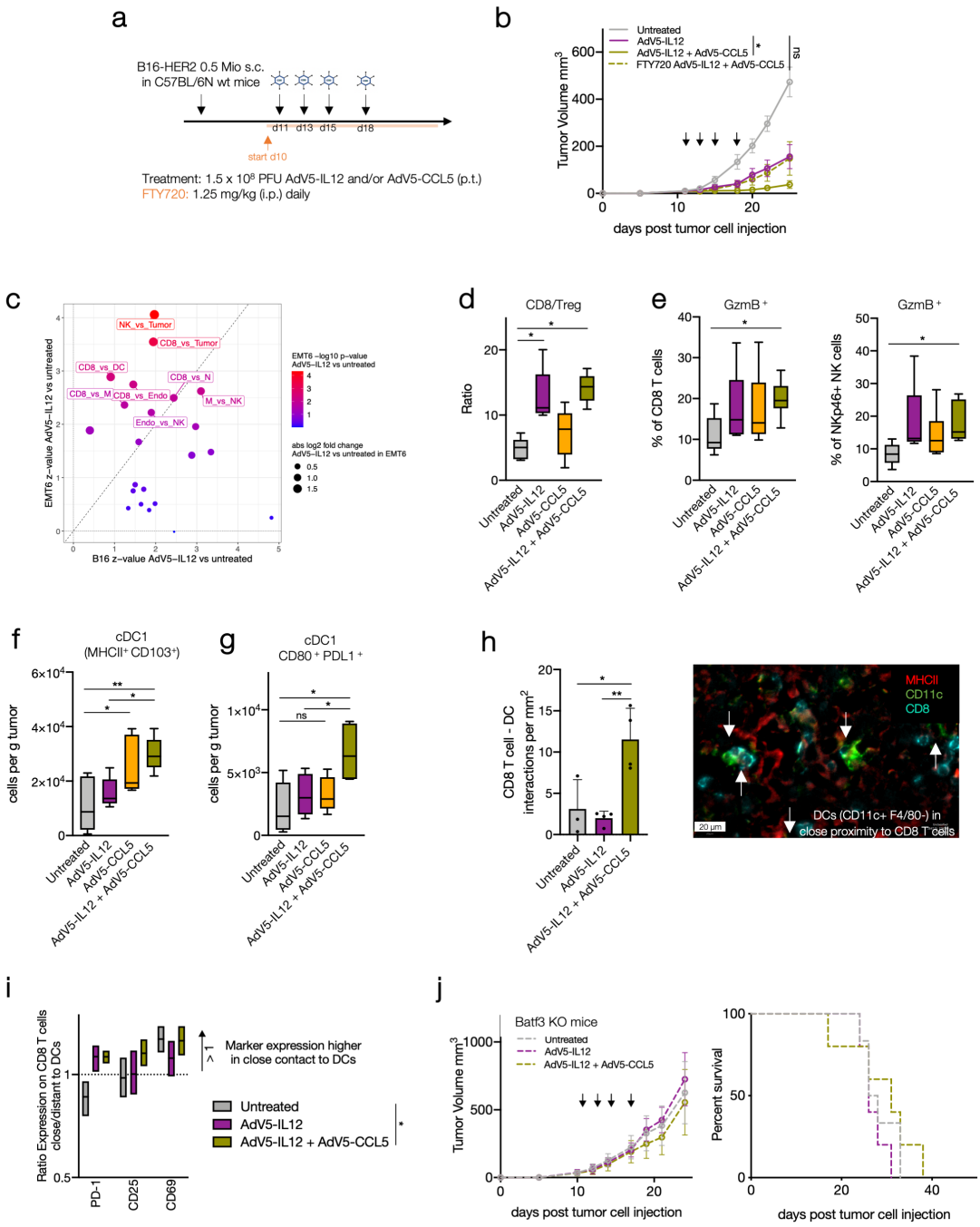

Figure 5: AdV5-CCL5 improves IL-12 response by inducing DC-CD8 T cell crosstalk

a-b: Mice were treated with AdV5-IL12 and AdV5-CCL5 on day 11, 13, 15 and 18 (tumor size 30–70 mm^3) after B16-HER2 inoculation. Lymphocyte trafficking was inhibited using FTY720 as indicated (orange arrow and line). Tumor growth curves are shown. Black arrows denote days of treatment. **c**: Wildtype (WT) mice were engrafted with 1 mio EMT6-HER2 (i.m.) or 0.5 Mio B16-HER2 (s.c.). Starting from day 7 or 11 (tumor size 30–70 mm^3), mice were treated with 1.5x10^8 PFU of HER2-targeted and shielded adenoviral vectors (p.t.) encoding for IL-12 on day 7/11, 9/13 and 11/15. On day 12/16 post inoculation, tumors were isolated, embedded in OCT and analyzed by multiparameter immuno-fluorescence microscopy. Visualization of odds ratios and p values for changes in cell-cell type interactions between EMT6-HER2 versus B16-HER2 focusing on interaction including CD8 T cells and NK cells. **d-i:** Wildtype (WT) mice were engrafted with

0.5 mio B16-HER2 (s.c.). Mice were treated with AdV5-IL12 and/or AdV5-CCL5 on day 11, 13 and 15 (tumor size 30–70 mm^3). On day 16 post inoculation, tumors were isolated and single cell suspensions were analyzed by flow cytometry or embedded in OCT and analyzed by multiparameter immunofluorescence microscopy. **d:** Ratio of CD8 T cells (CD8) versus regulatory T cells (Treg) (CD8: CD3+, CD4-, NKp46- CD19-; Treg: CD3+, CD4+, FOXP3+, CD25+, NKp46-, CD19-). **e:** Proportion of granzyme B+ of CD8 T cells (CD3+, CD4-, NKp46- CD19-) and NK cells (NKp46+, CD3-, Ly6G-, CD19-, F4/80-). **f-g:** Number of cDC1s (CD11c+, F4/80-, Ly-6G-, MHCII+, CD103+, $CD11b^{low}$) and PD-L1 and CD80 expressing cDC1s, respectively. **h:** Interaction count per mm^2 of CD8 T cells in close proximity to DCs. Representative IF pictures are showing AdV5-IL12 + AdV5-CCL5 treated tumors (MHCII: red, CD11c: green, CD8: blue). White arrows are showing CD8 T cells (CD45+, CD8+) neighboring DCs (CD45+, CD11c+, F4/80-). **i:** Ratio of PD-1, CD25 and CD69 expression on the CD8 T cell cluster in close (<50 µm) or distant (>50 µm) proximity to DC cluster. **j:** Batf3 knockout mice (lacking cDC1s) were engrafted with 0.5 mio B16-HER2 (s.c.). Mice were treated with AdV5-IL12 and/or AdV5-CCL5 as indicated (black arrows). Tumor growth and Kaplan-Meier survival curves are shown. **a-j:** n = 5-6 mice per group. *$p < 0.05$, **$p < 0.01$, ***$p < 0.001$, ****$p < 0.0001$. Error bar values represent SD or SEM (tumor growth curves). For comparisons between three or more groups, one-way ANOVA with multiple comparisons was used. For survival analysis, p values were computed using the Log Rank test. Two-way ANOVA was used to compare tumor growth curves. See also Extended data Fig. 3 and 6.

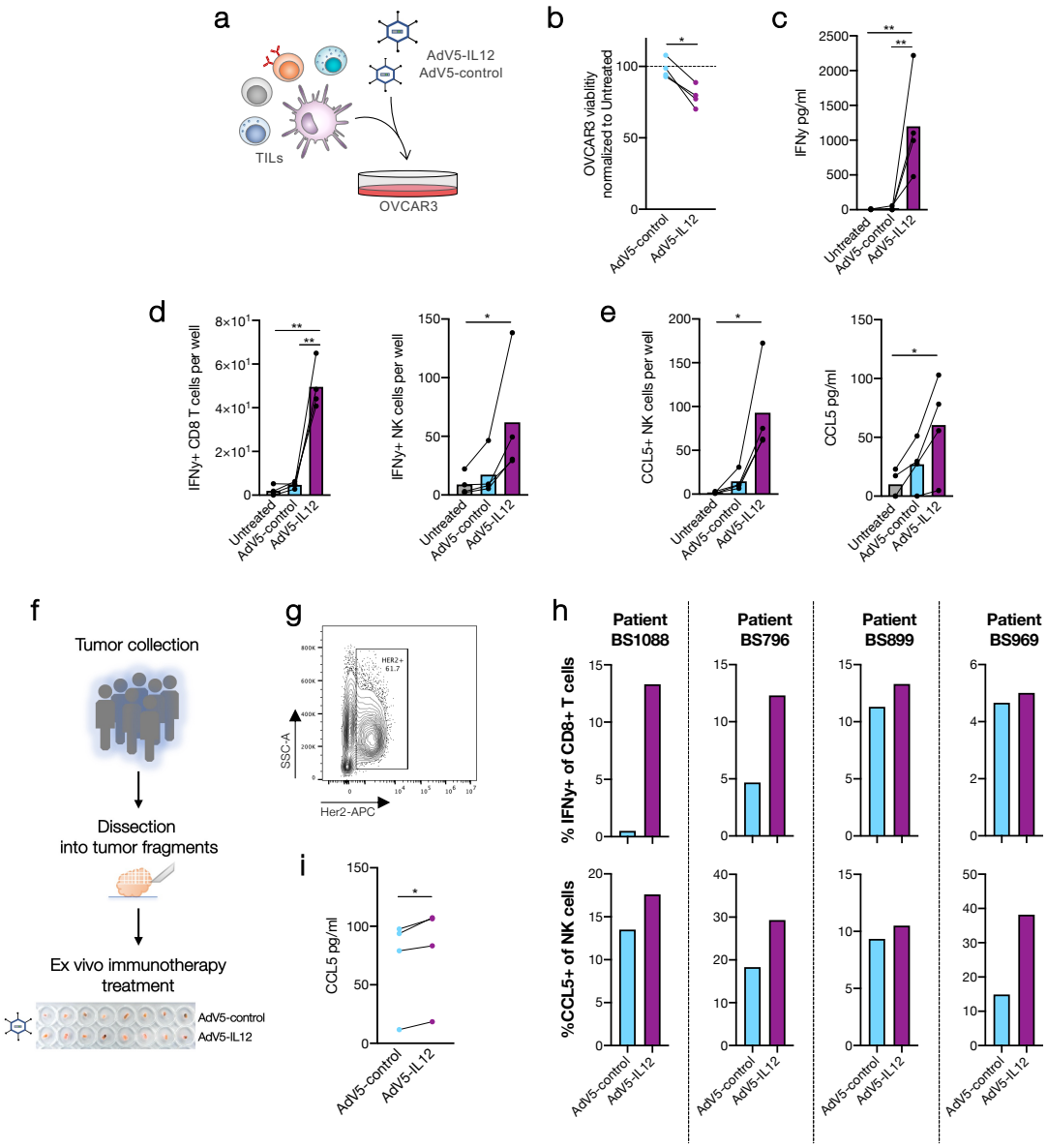

Figure 6: AdV5-hu-IL12 induces CCL5 expression in patient-derived tumor cultures

a-e: Tumor digests of NSCLC patients were co-cultured with OVCAR-3 cells which were transduced with HER2-targeted AdV5 encoding human IL-12 or control virus. **b:** Quantification of OVCAR-3 viability normalized to untreated co-cultures after 96 h. **c:** IFNγ expression was determined in supernatants after 5d. **d:** Cell count of IFNγ+ CD8 T cells (CD3+, CD56-) and NK cells (CD56+, CD3-) per well after 96 h. **e:** Cell count of CCL5+ NK cells (CD56+, CD3-) after 96 h and CCL5 expression in supernatants after 5d. **f-g:** HER2+ ovarian cancer samples were dissected into tumor fragments and cultivated embedded in matrigel. Tumor fragments were treated with HER2-targeted AdV5 encoding human IL-12 for 48 h (8-12 fragments per condition). **g:** Representative dot plot of HER2 expression analyzed by flow cytometry. **h:** After treatment tumor fragments per condition were pooled and analyzed by flow cytometry. Quantification of IFNγ+ CD8 T cells (CD3+, CD56-) and NK cells (CD56+, CD3-) after treatment. **I:** CCL5 concentration in supernatant was analyzed by ELISA. **a-g:** n = each 4 patients. *p < 0.05, **p < 0.01, ***p < 0.001, ****p

< 0.0001. 2-tailed paired Student's t test was used. For comparisons between three or more groups, paired one-way ANOVA with multiple comparisons was used. See also Extended data Fig. 7.

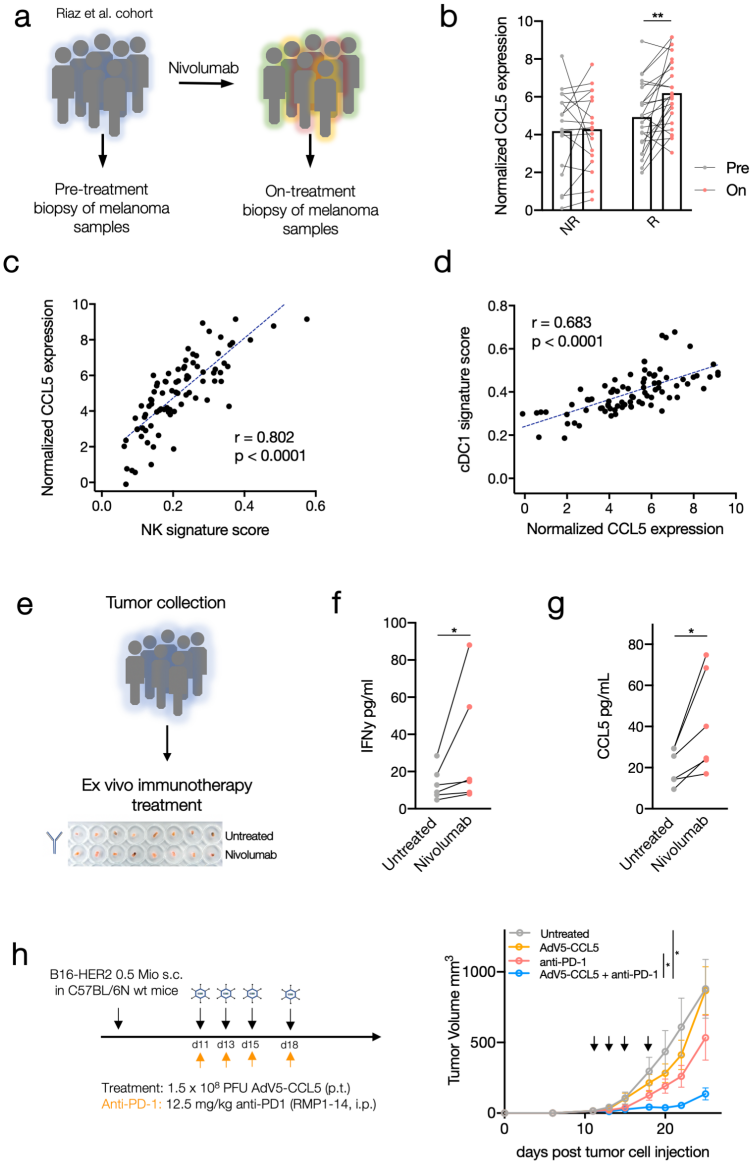

Figure 7: CCL5 expression is beneficial for anti-PD-1 efficacy

a-d: CCL5 expression in tumor biopsies of melanoma patients (n= 42) was analyzed pre and on nivolumab treatment [41]. **b** Comparison of CCL5 expression pre and on nivolumab treatment between patients with no response (NR) or response (R = SD+PR+CR). **c:** Correlation between CCL5 expression and NK signature score. **d:** Correlation between CCL5 expression and cDC1 signature score. **e-g:** Cancer samples were dissected into tumor fragments and cultivated embedded in Matrigel. Tumor fragments were treated with nivolumab for 48 h (6-8 fragments per condition). IFNγ and CCL5 were determined in the supernatant. n = 6 tumor samples. **h:** WT mice were engrafted with 0.5 mio B16-HER2 (s.c.). Mice were treated with AdV5-CCL5 (p.t.) and/or anti-PD-1 (i.p.) antibodies on day 11, 13, 15 and 18 (tumor size 30–70 mm^3) as indicated. Tumor growth curves are shown. n= 6 mice per condition. **a-f:** *p < 0.05, **p < 0.01, ***p < 0.001, ****p < 0.0001. Error bar values represent SEM. For comparisons between grouped data sets, two-way ANOVA with multiple comparisons was used. 2-tailed paired Student's t test was used. Two-way ANOVA was used to compare tumor growth curves.

Methods

Redesign of AdV5 shuttle vector

The pShuttle vector from the AdEasy™ Adenoviral Vector System (Agilent Technologies; Luo *et al.*, 2007) was redesigned to allow for the rapid generation and exchange of modular expression cassettes encoding a variety of payloads. The multiple cloning site (MCS) of the pShuttle vector was replaced with synthetic MCS modules, called MCS1 or MCS2, via Gibson Assembly (New England Biolabs). The synthetic MCS1 module contained, from 5' to 3', the CMV promoter, *NheI* restriction site, *XhoI* restriction site and the polyA site from BGH as previously described (Smith *et al.*, in press).The MCS2 module contained, from 5' to 3', the SV40 promoter, *SpeI* restriction site, *SalI* restriction site and the polyA site from SV40. MCS modules were synthesized by GeneArt (Life Technologies Europe BV) containing the N-terminal flanking DNA 5'-GAA TAA GAG GAA GTG AAA TCT GAA TAA TTT TGT GTT ACT CAT AGC GCG TAA -3,' and C-terminal flanking DNA 5'- TAA GGG TGG GAA AGA ATA TAT AAG GTG GGG GTC -3' for Gibson Assembly into pShuttle to generate the plasmids pShuttle-MCS1 or pShuttle-MCS2. Additionally, a plasmid called pShuttle-MCS1-MCS2 was constructed where both the MCS1 and MCS2 modules were inserted in tandem into the same pShuttle construct.

Construction of payload construct

Murine and human IL-12 constructs were generated from translated Genbank cDNA sequences for the IL-12B/p40 (NCBI Reference: BC103608.1 or BC074723.2, respectively) and IL-12A/p35 (NCBI Reference: BC146595.1 or BC104984.1, respectively) connected by a F2A peptide as previously described (Brücher *et al.*, 2021). The murine CCL5 gene was generated from Uniprot sequence P30882. Cytokines included their native signal sequences, were codon-optimized for human or mouse expression, respectively, and synthesized by GeneArt (Thermo Fisher Scientific). For reporter assays, a firefly luciferase reporter was synthesized from GenBank: BAL46512.1. Payload constructs were inserted into redesigned pShuttle vectors by Gibson assembly or standard ligation cloning to generate pShuttle-MCS1 including the payload. The pShuttle-MCS1 backbone (without payload) was used to generate the AdV5-control vector. In general, pShuttle-MCS1-IL12 (AdV5-IL12), pShuttle-MCS1-CCL5 (AdV5-CCL5) and pShuttle-MCS1-Luciferase (AdV5-Luc) were used to generate immunotherapeutic vectors. For the combinatorial approach optimization (Figure S5), pShuttle-MCS2-CCL5 (AdV5-SV40-CCL5) and pShuttle-MCS2-IL12 (AdV5-SV40-IL12), pShuttle-MCS1-IL12-MCS2-CCL5 (AdV5-CMV-IL12-SV40-CCL5) and pShuttle-MCS1-CCL5-MCS2-IL12 (AdV5-CMV-CCL5-SV40-IL12) were used.

Virus production

The plasmid containing the adenoviral genome, pAdEasy-1, from the AdEasy™ Adenoviral Vector System (Agilent Technologies; He *et al.*, 1998; Luo *et al.*, 2007) was previously modified to include a mutation to the hypervariable loop 7 (HVR7) of the hexon, which prevents blood factor X binding to virions and thus reduces liver infection [29]. To generate viral constructs, the modified pAdEasy-1_HVR7 plasmid was co-transformed with the pShuttle-MCS variants listed above into recA-proficient *E. coli* BJ5183 cells, from

which the desired recombinants, obtained by homologous recombination, could be isolated for virus production. Packaging and amplification of adenoviral particles was performed by Vector Biolabs (Malvern, PA, USA) and they were purified on two consecutive cesium chloride density gradients and provided directly in PBS with 5% glycerol.

Protein purification of adenoviral shield and retargeting adaptor

The human HER2 adenoviral retargeting adapter (G3_1D3nc_SHP1) was expressed and purified as previously described [29,47]. Endotoxin was removed from purified adapters using the Endotrap® HD Endotoxin Removal System (Hyglos GmbH) and adapters were stored at -80°C in endotoxin-free Dulbecco's PBS (Millipore TMS-012-A). The adenoviral shield was purified in *Sf9* insect cells as previously described [29].

Mice

C57BL/6 and Balb/c mice were bred in-house at University Hospital Basel, Switzerland. Batf3 KO (B6.129S(C)-Batf3<tm1Kmm>/J) mice were obtained from the Jackson laboratory, USA. Animals were housed under specific pathogen-free conditions. All animal experiments were performed in accordance with Swiss federal regulations. Sex-matched littermates at 8-12weeks of age at the start of experiments were used.

Tumor models

C57BL/6 and Batf3KO mice were injected subcutaneously into the right flank with 0.5 mio syngeneic murine B16 D5 melanoma cells expressing HER2 (kindly provided by Dr. L. Weiner, Georgetown University, Washington, DC) suspended in phenol red-free DMEM (without additives). EMT6 murine breast cancer cells expressing HER2 (1 mio; D'Amico *et al.*, 2019) were injected into the mammary gland of female Balb/c mice. Cell lines were tested for mycoplasma contamination before injection. Tumor volume was calculated according to the formula: D/2 x d x d, with D and d being the longest and shortest tumor diameter in mm, respectively.

Immunotherapy treatments

Tumor bearing mice, with a tumor size of approximately 30-70 mm^3, were treated with each $1.5x10^8$ PFU of HER2-targeted and shielded adenoviral vectors in 50 µl of PBS (peritumorally), and/or 12.5 mg/kg mouse anti-PD-1 (RPM1–14, BioXCell) or left untreated. For depletion studies, CD8 T cells were depleted by administering anti-CD8a (53-6.72, BioXCell) at 10mg/kg (i.p.) once per week. NK depletion was performed by administering anti-Asialo-GM1 (Poly21460, Biolegend) 50 µl (i.p.) in Balb/c mice or anti-NK1.1 (PK136, BioXCell) 10 mg/kg (i.p.) in C57BL/6 mice every 4-5 days. IFNγ neutralization was performed using anti-IFNγ antibody (XMG1.2, BioXcell) at 25 mg/kg in 200 µl PBS injected every 2-3 days. To neutralize CCL5, we injected 32 µg anti-CCL5 antibody (500-P118, Peprotech) in 200 µl PBS per

mouse intraperitoneally. Depletion and neutralization schedules were started the day before immunotherapy treatment unless stated otherwise.

Bilateral tumor models

Balb/c mice were inoculated with 1 mio EMT6-HER2 tumor cells (i.m.) in the right flank. Four days later, 0.25 mio EMT6 wt cells were injected in the contralateral site (i.m.). On day 7, 9, 11 and 13 post first tumor inoculation, EMT6-HER2 tumors were treated with each $1.5x10^8$ PFU of HER2-targeted and shielded adenoviral vector encoding IL-12 in 50 µl of PBS (peritumorally). Tumor volumes of contralateral (EMT6 wt) tumors were measured.

Tumor re-challenge

Long-term surviving mice from AdV5-IL12 therapy were re-challenged with EMT6 wt and EMT6-HER2 tumors in each flank 60 days after primary tumor rejection. EMT6 wt and EMT6-HER2 re-challenge doses were 0.25 mio cells and 1 mio cells, respectively. As a control, naive Balb/c mice were implanted alongside re-challenged mice.

FTY720 treatments

Mice were implanted with EMT6-HER2 or B16-HER2 tumors intramammarily or subcutaneously, respectively. Mice were treated or not with 1.25 mg/kg of FTY720 (Cayman Chemical) i.p. daily throughout the duration of the experiment. Injections were started one day before tumor inoculation or the day before adenoviral treatment.

In vivo pharmacokinetic experiments

Mice were implanted with EMT6-HER2 or B16-HER2 tumors intramammarily or subcutaneously, respectively. Once the tumors reached an average volume of 30-70 mm^3, luciferase-encoding retargeted and shielded AdV5 ($1.5x10^8$ PFU per mouse; AdV5-Luc) were injected peritumorally. The luciferase signal was determined in live animals one day after virus injection and 10 minutes after intraperitoneal injection of 150 mg/kg D-luciferin (PerkinElmer) using the in vivo imaging system NightOWL II LB 983 (Berthold) over two weeks. Following live imaging, luciferase activity was determined in isolated tumors and organs (draining and non-draining lymph nodes, spleen, liver, kidney, lung and heart). The overlay of the real image and the luminescence representation allowed the localization and measurement of luminescence emitted from xenografts. The signal intensities from manually derived regions of interest (ROI) were obtained and data were expressed as photon flux (photon/s). All measurements were performed under the same conditions, including camera settings, exposure time (60 s), distance from lenses to the animals and ROI size.

Multiparameter flow cytometry

Tumor tissue was isolated from mice, weighed and minced using razor blades. Tissue was then digested using accutase (PAA), collagenase IV (Worthington), hyaluronidase (Sigma), and DNAse type IV (Sigma) for 60 min at 37°C with constant shaking. The cell suspensions were filtered using a cell strainer (70 µm). Precision Counting beads (Biolegend) were added before staining to quantify the number of cells per gram tumor. Single cell suspensions were blocked with rat anti-mouse FcγIII/II receptor (CD16/CD32) blocking antibodies ("Fc-Block") and stained with live/dead cell-exclusion dye (Zombie UV dye; Biolegend). The cells were then incubated with fluorophore-conjugated antibodies directed against cell surface antigens, washed and resuspended in FACS buffer (PBS + 2% FBS). For intracellular/intranuclear antigens, cells stained with cell surface antibodies were fixed and permeabilized using Foxp3/transcription factor staining buffer set (eBioscience) prior to incubation with antibodies directed against intracellular antigens. Cell populations were analyzed on a Cytek Aurora and Cytoflex.

Bioinformatic analysis of flow cytometry data

FCS files containing pre-gated alive CD45+ single cells were read into R using the flowCore package (*flowCore: flowCore: Basic structures for flow cytometry data version 2.2.0 from Bioconductor*). A logicle transform was performed per channel, with parameters calculated from aggregated data from all samples. CD45 low cells with a transformed value of < 2.5 were removed from further analysis (threshold set on left side of trough of density plot of transformed CD45 values from all samples). The measurements were randomly subsampled to 1.5 x 10^5 cells per condition to expedite downstream operations. Principal Component Analysis (PCA) was performed using all markers except for CD45, Live-Dead, FSC* and SSC*.Uniform Manifold Approximation and Projection (UMAP) was performed for visualization using the CATALYST module's runDR function (*CATALYST: Cytometry dATa anALYSis Tools version 1.14.0 from Bioconductor*). Clustering was performed using Rphenograph (0.99.1), an R implementation of PhenoGraph (*GitHub - JinmiaoChenLab/Rphenograph: Rphenograph: R implementation of the PhenoGraph algorithm*; Levine *et al.*, 2015). Five clusters with universally high expression across all markers were removed, and steps starting with PCA were repeated. Three resulting clusters were again removed and the process iterated once more to yield the final clustering, UMAP and heatmaps [77]. Supplemental UMAP visualization of scaled marker expression done with CATALYST's plotDR function. Main cell types were assigned by marker expression. To confirm certain assignments, cell populations were gated using FlowJo (10.6.2) and compared to assigned populations (e.g. NK cells: NKp46+, CD3-, CD19- Ly-6G-, F4/80-).

Multiparameter fluorescence microscopy

Tumors embedded in OCT were sectioned into 7 µm-thick slices and attached to poly-L-lysine coated square coverslips. Sections were analyzed using CODEX® (Akoya Biosciences), a highly multiplexed imaging platform, which allows the staining of solid tissue sections with a panel of up to 40 antibodies at once [35]. In brief, CODEX uses a unique DNA barcode system to label each antibody clone individually. These barcodes can be detected by reversible hybridization to its corresponding reporter. The respective

reporters, which are conjugated with the fluorophores AF488, Atto550 or Cy5, are applied onto the tissue sections, imaged and removed in a multicycle experiment. For this purpose, the manufacturer's protocol "CODEX User Manual Rev A.0" (provided by AKOYA Biosciences) was followed.

The antibody panel was composed of commercially available AKOYA-conjugated antibodies and self-conjugated custom antibodies (CODEX Conjugation Kit, AKOYA Biosciences). Tissue staining was performed with the CODEX Staining Kit (AKOYA Biosciences). Briefly, the tissue was thawed with drierite beads, fixed with acetone, rehydrated and fixed with 1.6% paraformaldehyde (PFA). After blocking, the tissue was stained with the established antibody panel consisting of 33 barcoded antibodies at the same time. The bound antibodies were fixed to the tissue with 1.6% PFA, ice-cold methanol and a fixative solution (AKOYA Biosciences).

The inverse microscope DMi8 (Leica) was used for acquisition (20x magnification, xyz acquisition mode 14 Z-stacks each 14.99 µm, "Best Focus" autofocus with default settings). The generated fluorescence data were formatted with the Akoya CodexDriver V2 and subsequently processed using CODEX Processor (Version v1.5.0.48b) or the Kheops PlugIn in ImageJ and QuPath0.2.3 and StarDist [78–80]. The processing steps included 1) XY Processing with tile registration and shading correction; 2) Z-Stack Processing with deconvolution, drift compensation, overlap cropping, background subtraction (min-min mode) and best focus detection; 3) Stitching with best focus interpolation and tile overlap of 10% and 4) Cell segmentation on the nuclear stain with the radius 8 or threshold (0.69), channels ('DAPI'), normalize percentiles (1.99), pixel size (0.423), cell Expansion (2.8), cell constrain scale (1.5) in StarDist, respectively.

The processed and segmented data were analyzed with the CODEX Multiple Analysis Viewer (Version 1.2.0.297) or the PhenoGraph algorithm using R 4.0.2. Manual gating was performed to distinguish between CD45+ cells (immune cells) and CD45- cells (tumor and stroma cells). Clustering was performed with VORTEX using unbiased hierarchical X-shift clustering (K = 55 resulting in 81 immune clusters; Samusik *et al.*, 2016). Clusters were manually verified and assigned to main immune cell populations using CODEX Multiple Analysis Viewer or QuPath. Subsequently, mean marker expression and interaction counts between cellular main populations (cells with <50 µm proximity) were determined.

Interaction analysis

Interaction counts between main cell populations (contact defined as <50 µm proximity) were used for further analysis. The cluster "L" containing lymph vessels was excluded from further analysis, because of the very distinct localization of its cells as small vessels. Expected interaction counts for each cell-cell interaction pair were calculated as:

$$expectedInteractions_{CellA\_CellB} = interactions_{allCells} * frequency_{CellA} * frequency_{CellB}$$

Next a negative-binomial generalized linear model for the interaction counts with an offset of log(expectedInteractions) was generated in R 4.0.2. The mathematical interaction terms between cell-cell type comparison (e.g. DC_vs_CD8) and experimental condition (untreated, AdV5-empty, AdV5-IL12) were

used to calculate odds ratios and p-values for changes in cell-cell type interactions between experimental conditions. Odds ratios for different subsets of immune cells were plotted using ggplot2.

Intra-tumoral and systemic cytokine measurements

Serum was collected in EDTA containing tubes (Sarstedt) and IL-12 levels were determined using the IL-12 p70 Mouse Uncoated ELISA Kit (Invitrogen). Isolated tumors were snap-frozen on dry ice. Before thawing, a 5 mm metal bead and 1 ml of lysis buffer (20 mM Tris HCl (pH 7.5), 0.5% Tween 20, 150 mM NaCl, Sigma protease inhibitors 1:100) were added to the tubes. Tumors were lysed using a TissueLyser (Qiagen) for 5 min at 25 Hz. After centrifugation, protein concentrations were determined with the Pierce BCA Protein Assay Kit (Thermo Scientific). CCL5 concentration in the tumor lysates were analyzed by ELISA (Mouse RANTES Uncoated ELISA Kit Invitrogen) and normalized to the determined total protein concentrations.

Patients and sample preparation

Surgical specimens were mechanically dissociated, digested with accutase (PAA Laboratories), collagenase IV (Worthington), hyaluronidase (MilliporeSigma), and DNAse type I (MilliporeSigma), filtered, washed and frozen as single cell suspension for future use. For human ex vivo tumor cultures, surgical specimens were dissected into tumor fragments and frozen for future use. Human PBMCs were isolated by density gradient centrifugation using Histopaque-1077 (MilliporeSigma) from buffy coats obtained from healthy blood donors (Blood Bank, University Hospital Basel). PBMCs were frozen for later use in liquid nitrogen. Ethics approval was obtained from the local ethical committee to analyze the tissue and blood samples (Ethikkommission Nordwestschweiz) and written informed consent was obtained from all patients prior to sample collection.

Ex vivo human immune cells and tumor co-culture experiments

Healthy donor PBMCs or tumor digest samples, processed as described above, were co-cultured with OVCAR3 human ovarian cancer cell line, similarly to as described in Natoli *et al*. 2020. Briefly, 6000 OVCAR3 cells were seeded on the wells of a flat-bottom 96-well plate in RPMI containing L-glutamine (R8758, Sigma-Aldrich), supplemented with penicillin/streptomycin (100 ng/ml, Sigma-Aldrich) and 10% FBS (Sigma-Aldrich). After 2 hours, the medium was replaced with fully supplemented RPMI containing AdV5-hu-IL12 or empty vector control (AdV5-control) at a PFU of 1000/cell. Additional control wells were left untreated. After 2 hours of incubation, the medium was replaced to remove the virus and the tumor cells were incubated for 2 days at 37°C, 5% CO2. 300,000 healthy donor PBMCs or single cells from tumor digest samples were then added to the wells of the 96-well plate in a final volume of 200 µl per well. Tumor cell (OVCAR3) viability was assessed by an MTT assay and flow cytometry was conducted on the suspension cells (PBMCs, TILs) after 3 days of co-culture. The supernatant was collected after 6 days of co-culture to assess IFNγ and CCL5 levels using a Human IFNγ ELISA Set (BD OptEIA, 555142) and ELISA

MAX™ Deluxe Set Human CCL5 (Biolegend, 440804), respectively, according to the manufacturers' instructions.

Ex vivo tumor fragment culture

Tumor fragment cultures were prepared as described in Voabli *et al*. in press. Briefly, frozen patient tumor fragments were slowly thawed at 37°C and extensively washed in PBS and warm RPMI medium containing L-glutamine (R8758, Sigma-Aldrich), supplemented with penicillin/streptomycin (100 ng/ml, Sigma-Aldrich), 10% FBS (Sigma-Aldrich), 1x MEM Non-Essential Amino Acids (Gibco) and 1 mM sodium pyruvate (Sigma-Aldrich).

Single tumor fragments were then embedded in a total of 80 µl of an artificial extracellular matrix within the wells of a flat-bottom 96-well plate. The extracellular matrix was prepared by mixing ice-cold sodium bicarbonate (Sigma; 1.1% final concentration), collagen I (Corning; 1 mg/ml final concentration) and fully supplemented RPMI with ice-cold matrigel (Matrix High Concentration, Phenol Red-Free, BD Biosciences; 4 mg/ml final concentration). 40 µl of matrix was solidified by incubation at 37°C for 20-30 min. One tumor fragment per well was placed on top of the pre-solidified matrix, after which a second layer of 40 µl matrix was added. Plates were then placed in a 37°C incubator for further 20-30 min. 110 µl of fully supplemented RPMI was added on top of the matrix. 1 mio PFU of AdV5-hu-IL12 or control AdV5-control or nivolumab (10 µg/ml final concentration) were added to each well containing individual tumor fragments. Between 6-12 fragments were used for each treatment conditions. After 48 hours of incubation at 37°C, the fragments were pooled and enzymatically digested and filtered into single cell suspensions, as described above. Flow cytometry was conducted and the supernatant was collected from each well to assess IFNγ and CCL5 levels using a Human IFNγ ELISA Set (BD OptEIA, 555142) and ELISA MAX™ Deluxe Set Human CCL5 (Biolegend, 440804), respectively, according to the manufacturers' instructions.

MTT assay

To assess tumor cell viability in co-culture experiments, an MTT assay was used as follows. The medium from the co-culture wells was removed and the wells were gently washed once with PBS to remove suspension cells. MTT (Sigma-Aldrich) was then added at 500 µg/ml and the tumor cells were incubated at 37°C for 2–3 hours. Formazan crystals were resuspended in 90 µl of dimethyl sulfoxide (DMSO; Sigma-Aldrich) and absorbance was measured at a wavelength of 570 nm.

Bioinformatic analysis of published gene expression data of human melanoma samples

We received the normalized Nanostring RNA expression data from the NCT01502293 trial (Oncosec), in which patients received IL-12-encoding mRNA by intra-tumoral electroporation [20]. The gene signatures for different immune sub-populations were retrieved from the PanCancerImmunology Nanostring panel. The transcripts within the "Cytotoxic cells" signature can't be attributed to a single cell type and are found in other signature lists of both NK and CD8 T cells. Therefore, its transcripts were merged with the cytotoxic NK and CD8 T cells resulting in the "Cytotoxic CD8+ T cells" and "Cytotoxic NK cells" signatures.

Importantly, neither "Cytotoxic CD8+ T cells" and "Cytotoxic NK cells" contained the CCL5 transcript. Downstream analysis of all Nanostring data was performed using R version 4.0.2 and visualized in GraphPad Prism 9.

Immune cell infiltration was estimated by calculating a signature score as described by Cursons et al. 2019. Briefly, all transcripts for each sample were ordered by decreasing expression and the signature score was defined as:

$$1 - \frac{mean\ rank\ of\ signature\ transcripts}{number\ of\ all\ transcripts}$$

Thus, a high signature score indicates enrichment of signature transcripts among genes with high expression. To find genes that correlate with the Cytotoxic NK cells signature score, we performed a linear regression for signature scores with log-transformed transcript counts. p-values were adjusted by the Benjamini-Hochberg correction method.

We also reanalyzed RNAseq data of samples from tumor patients treated with anti-PD-1 antibodies (nivolumab; Riaz *et al.*, 2017). Data was downloaded from the GEO under accession number GSE91061. Only patients with both pre- and post-treatment samples and evaluated responses were analyzed. Counts were normalized by library size using edgeR and displayed as log counts per million using GraphPad Prism 9. Paired two-way ANOVA with multiple comparisons and the post-hoc test were used to calculate significances for increased CCL5 expression upon treatment in CB. The availability of RNAseq data allowed the use of more complex gene signatures than with Nanostring data above. Therefore, we used the signatures described by Tirosh et al and Cursons et al. for this analysis [82,83]. As we wanted to correlate signatures with CCL5 expression, CCL5 was excluded from the T cell signature provided by Tirosh et al. 2016. Signature scores were calculated as described above.

Statistical Analysis

For normally-distributed datasets, we used 2-tailed Student's t test and one-way ANOVA followed by Holm-Sidak multiple comparison test. When variables were not normally distributed, we performed non-parametric Mann-Whitney or Kruskal-Wallis tests. For survival analysis, p values were computed using the Log Rank test. Two-way ANOVA was used to compare tumor growth curves and grouped data sets. p values > 0.05 were considered not significant, p values < 0.05 were considered significant. * p value < 0.05, ** p value < 0.01, *** p value < 0.001, **** p value < 0.0001.

Reporting Summary

Further information on research design is available in the Nature Research Reporting Summary linked to this article.

Data availability

The previously published RNAseq data we re-analyzed is accessible at GEO under accession number GSE91061. Source data and all other supporting data of this study are available from the corresponding authors on a reasonable request.

Code availability

Codes used for the analysis of flow cytometry data and multidimensional IF microscopy in Fig. 2, as well as the analysis of published expression data in Fig. 3 and Fig. 6 can be obtained from the corresponding authors upon request.

Acknowledgments

We thank members of the Cancer Immunology and Cancer Immunotherapy Laboratory at the Department of Biomedicine for helpful discussions and suggestions. We are grateful to A. Ignatenco and B. Simic for cloning viral constructs and to F. Weiss, and P. Freitag for producing and providing the biological reagents. We thank Priska Auf der Maur (University Hospital of Basel) for designing the graphical abstract. This work benefited from clinical data provided by OncoSec Medical Incoporated. This work was funded by the Schweizerische Nationalfonds Grant CRSII5_170929 to A.Z. and A.P., by the Schweizerische Nationalfonds Grant 320030_188576/1 to A.Z. and by the National Cancer Institute of the National Institutes of Health under award number F32CA189372 (to S.N.S.), and by the University of Zurich Forschungskredit 2017 ID 3761 (to D.B.).

Authors contributions

N.K. designed the study, performed experiments, analyzed data, and wrote the manuscript. M.P.T., M.N., F.W., V.K., M.B. and D.S.T. planned and performed experiments and generated and analyzed data. D.B., S.N.S., D.B., K.P.H and P.Z. designed, cloned or produced biological reagents. D.S. and E.B. processed and analyzed data. M.P.T., M.N., D.B., S.N.S., H.L., M.A.S., A.S.K. and A.P. provided input for research design and interpretation and edited the manuscript. A.Z. directed the study and wrote the manuscript. All authors reviewed and approved the manuscript.

Declaration of Interests

The authors declare no competing interests.

References

1. Ribas, A. & Wolchok, J. D. Cancer immunotherapy using checkpoint blockade. *Science* **359**, 1350–1355 (2018).
2. Wolchok, J. D. *et al.* Overall Survival with Combined Nivolumab and Ipilimumab in Advanced Melanoma. *N. Engl. J. Med.* **377**, 1345–1356 (2017).
3. Hegde, P. S. & Chen, D. S. Top 10 Challenges in Cancer Immunotherapy. *Immunity* **52**, 17–35 (2020).
4. Kalbasi, A. & Ribas, A. Tumour-intrinsic resistance to immune checkpoint blockade. *Nature Reviews Immunology* **20**, 25–39 (2020).
5. Waldman, A. D., Fritz, J. M. & Lenardo, M. J. A guide to cancer immunotherapy: from T cell basic science to clinical practice. *Nature Reviews Immunology* **20**, 651–668 (2020).
6. Barry, K. C. *et al.* A natural killer–dendritic cell axis defines checkpoint therapy–responsive tumor microenvironments. *Nat. Med.* **24**, 1178–1191 (2018).
7. Gardner, A., de Mingo Pulido, Á. & Ruffell, B. Dendritic Cells and Their Role in Immunotherapy. *Front. Immunol.* **11**, 1–14 (2020).
8. Huntington, N. D., Cursons, J. & Rautela, J. The cancer–natural killer cell immunity cycle. *Nat. Rev. Cancer* **20**, 437–454 (2020).
9. Garris, C. S. *et al.* Successful Anti-PD-1 Cancer Immunotherapy Requires T Cell-Dendritic Cell Crosstalk Involving the Cytokines IFN-γ and IL-12. *Immunity* (2018). doi:10.1016/j.immuni.2018.09.024
10. Tugues, S. *et al.* New insights into IL-12-mediated tumor suppression. *Cell Death Differ.* **22**, 237–246 (2015).
11. Ruffell, B. *et al.* Macrophage IL-10 Blocks CD8+ T Cell-Dependent Responses to Chemotherapy by Suppressing IL-12 Expression in Intratumoral Dendritic Cells. *Cancer Cell* **26**, 623–637 (2014).
12. Ayers, M. *et al.* IFN-γ-related mRNA profile predicts clinical response to PD-1 blockade. *J. Clin. Invest.* **127**, 2930–2940 (2017).
13. Böttcher, J. P. *et al.* NK Cells Stimulate Recruitment of cDC1 into the Tumor Microenvironment Promoting Cancer Immune Control. *Cell* **172**, 1022-1037.e14 (2018).
14. Cursons, J. A gene signature predicting natural killer cell infiltration and improved survival in melanoma patients. *Cancer Immunol. Res.* **7**, 1162–1174 (2019).
15. Zhao, Y. *et al.* PD-L1:CD80 Cis-Heterodimer Triggers the Co-stimulatory Receptor CD28 While Repressing the Inhibitory PD-1 and CTLA-4 Pathways. *Immunity* **51**, 1059-1073.e9 (2019).
16. Lee, H. Integrated molecular and immunophenotypic analysis of NK cells in anti-PD-1 treated metastatic melanoma patients. *Oncoimmunology* **8**, (2019).
17. Weiss, G. R. *et al.* Phase 1 Study of the Intravesical Administration of Recombinant Human Interleukin-12 in Patients With Recurrent Superficial Transitional Cell Carcinoma of the Bladder. *J. Immunother.* **26**, 343–348 (2003).
18. Hurteau, J. A., Blessing, J. A., DeCesare, S. L. & Creasman, W. T. Evaluation of recombinant human interleukin-12 in patients with recurrent or refractory ovarian cancer: A gynecologic oncology group study. *Gynecol. Oncol.* **82**, 7–10 (2001).
19. Nguyen, K. G. *et al.* Localized Interleukin-12 for Cancer Immunotherapy. *Front. Immunol.* **11**, 1–36 (2020).
20. Algazi, A. *et al.* Intratumoral delivery of tavokinogene telseplasmid yields systemic immune responses in metastatic melanoma patients. *Ann. Oncol.* (2019). doi:10.1016/j.annonc.2019.12.008
21. Strauss, J. *et al.* First-in-human phase I trial of a tumor-targeted cytokine (NHS-IL12) in subjects with metastatic solid tumors. *Clin. Cancer Res.* **25**, 99–109 (2019).

22. Sangro, B. *et al.* Phase I trial of intratumoral injection of an adenovirus encoding interleukin-12 for advanced digestive tumors. *J. Clin. Oncol.* **22**, 1389–1397 (2004).

23. Hamid, O. *et al.* 19O Preliminary safety, antitumor activity and pharmacodynamics results of HIT-IT MEDI1191 (mRNA IL-12) in patients with advanced solid tumours and superficial lesions. *Ann. Oncol.* **32**, S9 (2021).

24. Motzer, R. J. *et al.* Nivolumab plus Ipilimumab versus Sunitinib in Advanced Renal-Cell Carcinoma. *N. Engl. J. Med.* **378**, 1277–1290 (2018).

25. Hellmann, M. D. *et al.* Nivolumab plus Ipilimumab in Advanced Non–Small-Cell Lung Cancer. *N. Engl. J. Med.* **381**, 2020–2031 (2019).

26. Galon, J. & Bruni, D. Approaches to treat immune hot, altered and cold tumours with combination immunotherapies. *Nat. Rev. Drug Discov.* **18**, 197–218 (2019).

27. Smith, S. N. *et al.* The SHREAD gene therapy platform for paracrine delivery improves tumor localization and 3 intratumoral effects of a clinical antibody. *Proc. Natl Acad. Sci. USA* (2021).

28. Brücher, D. *et al.* iMATCH: an integrated modular assembly system for therapeutic combination high-capacity adenovirus gene therapy. *Mol. Ther. - Methods Clin. Dev.* **20**, 572–586 (2021).

29. Schmid, M. *et al.* Adenoviral vector with shield and adapter increases tumor specificity and escapes liver and immune control. *Nat. Commun.* **9**, 1–16 (2018).

30. Brummelman, J. High-dimensional single cell analysis identifies stem-like cytotoxic CD8+ T cells infiltrating human tumors. *J. Exp. Med.* **215**, 2520–2535 (2018).

31. Jeannet, G. Essential role of the Wnt pathway effector Tcf-1 for the establishment of functional CD8 T cell memory. *Proc. Natl Acad. Sci. USA* **107**, 9777–9782 (2010).

32. Kurtulus, S. Checkpoint blockade immunotherapy induces dynamic changes in PD-1–CD8+ tumor-infiltrating T cells. *Immunity* **50**, 181–194 (2019).

33. Sade-Feldman, M. Defining T cell states associated with response to checkpoint immunotherapy in melanoma. *Cell* **175**, 998–1013 (2018).

34. Siddiqui, I. Intratumoral Tcf1+PD-1+CD8+ T cells with stem-like properties promote tumor control in response to vaccination and checkpoint blockade immunotherapy. *Immunity* **50**, 195-211.e10 (2019).

35. Goltsev, Y. *et al.* Deep Profiling of Mouse Splenic Architecture with CODEX Multiplexed Imaging. *Cell* **174**, 968-981.e15 (2018).

36. Morris, M. A. *et al.* Transient T cell accumulation in lymph nodes and sustained lymphopenia in mice treated with FTY720. *Eur. J. Immunol.* **35**, 3570–3580 (2005).

37. Müller, P. *et al.* Trastuzumab emtansine (T-DM1) renders HER2+ breast cancer highly susceptible to CTLA-4/PD-1 blockade. *Sci. Transl. Med.* **7**, (2015).

38. Hildner, K. *et al.* Batf3 deficiency reveals a critical role for CD8α+ dendritic cells in cytotoxic T cell immunity. *Science (80-.).* **322**, 1097–1100 (2008).

39. Natoli, M., Bonito, N., Robinson, J. D., Ghaem-Maghami, S. & Mao, Y. Human ovarian cancer intrinsic mechanisms regulate lymphocyte activation in response to immune checkpoint blockade. *Cancer Immunol. Immunother.* **69**, 1391–1401 (2020).

40. Voabil, P. *et al.* Immunological response of human cancers to PD-1 blockade. *Nat. Med.*

41. Riaz, N. *et al.* Tumor and Microenvironment Evolution during Immunotherapy with Nivolumab. *Cell* **171**, 934-949.e15 (2017).

42. Mokhtari, R. B. *et al.* Combination therapy in combating cancer. *Oncotarget* **8**, 38022–38043 (2017).

43. Sun, J. *et al.* A systematic analysis of FDA-approved anticancer drugs. *BMC Syst. Biol.* **11**, (2017).

44. Meric-Bernstam, F., Larkin, J., Tabernero, J. & Bonini, C. Enhancing anti-tumour efficacy with immunotherapy combinations. *Lancet* (2020). doi:10.1016/s0140-6736(20)32598-8

45. Algazi, A. P. *et al.* Phase II Trial of IL-12 Plasmid Transfection and PD-1 Blockade in Immunologically Quiescent Melanoma. *Clin. Cancer Res.* **26**, 2827–2837 (2020).

46. Riley, R. S., June, C. H., Langer, R. & Mitchell, M. J. Delivery technologies for cancer immunotherapy. *Nature Reviews Drug Discovery* **18**, 175–196 (2019).

47. Dreier, B. *et al.* Development of a generic adenovirus delivery system based on structure-guided design of bispecific trimeric DARPin adapters. *Proc. Natl. Acad. Sci. U. S. A.* **110**, (2013).

48. Dreier, B. & Plückthun, A. Rapid selection of high-affinity binders using ribosome display. *Methods Mol. Biol.* **805**, 261–286 (2012).

49. Plückthun, A. Designed ankyrin repeat proteins (DARPins): Binding proteins for research, diagnostics, and therapy. *Annual Review of Pharmacology and Toxicology* **55**, 489–511 (2015).

50. Yan, M., Parker, B. A., Schwab, R. & Kurzrock, R. HER2 aberrations in cancer: Implications for therapy. *Cancer Treatment Reviews* **40**, 770–780 (2014).

51. Kakarla, S., Song, X. T. & Gottschalk, S. Cancer-associated fibroblasts as targets for immunotherapy. *Immunotherapy* **4**, 1129–1138 (2012).

52. Trüb, M. *et al.* Fibroblast activation protein-targeted-4-1BB ligand agonist amplifies effector functions of intratumoral T cells in human cancer. *J Immunother Cancer* **8**, 238 (2020).

53. Brücher, D. *et al.* iMATCH - an integrated modular assembly-system for therapeutic 2 combination high-capacity adenovirus gene therapy. *Mol. Ther. - Methods Clin. Dev.* (2021).

54. Muruve, D. *et al.* The inflammasome recognizes cytosolic microbial and host DNA and triggers an innate immune response. *nature.com*

55. Appledorn, D. M., Patial, S., Godbehere, S., Parameswaran, N. & Amalfitano, A. TRIF, and TRIF-interacting TLRs differentially modulate several adenovirus vector-induced immune responses. *J. Innate Immun.* **1**, 376–388 (2009).

56. Andrea Amalfitano Godbehere, and, Van Rooijen, N., Parameswaran Daniel Appledorn, N. M., Patial, S. & McBride, A. Vivo Dependent upon Both TLR2 and TLR9 In As Well As Adaptive Immune Responses Are Inflammatory Mediators, MAPK Signaling, Adenovirus Vector-Induced Innate. *Am Assoc Immnol* (2021). doi:10.4049/jimmunol.181.3.2134

57. Urban-Wojciuk, Z. *et al.* The role of tlrs in anti-cancer immunity and tumor rejection. *Front. Immunol.* **10**, 2388 (2019).

58. Budhwani, M., Mazzieri, R. & Dolcetti, R. Plasticity of type I interferon-mediated responses in cancer therapy: From anti-tumor immunity to resistance. *Frontiers in Oncology* **8**, 322 (2018).

59. Zilionis, R. *et al.* Single-Cell Transcriptomics of Human and Mouse Lung Cancers Reveals Conserved Myeloid Populations across Individuals and Species. *Immunity* **50**, 1317-1334.e10 (2019).

60. Motzer, R. J. *et al.* Randomized multicenter phase II trial of subcutaneous recombinant human interleukin-12 versus interferon-α2a for patients with advanced renal cell carcinoma. *J. Interf. Cytokine Res.* **21**, 257–263 (2001).

61. Spranger, S., Dai, D., Horton, B. & Gajewski, T. F. Tumor-Residing Batf3 Dendritic Cells Are Required for Effector T Cell Trafficking and Adoptive T Cell Therapy. *Cancer Cell* **31**, 711-723.e4 (2017).

62. Prat, A. *et al.* Immune-related gene expression profiling after PD-1 blockade in non–small cell lung carcinoma, head and neck squamous cell carcinoma, and melanoma. *Cancer Res.* **77**, 3540–3550 (2017).

63. Murooka, T. T., Rahbar, R. & Fish, E. N. CCL5 promotes proliferation of MCF-7 cells through mTOR-dependent mRNA translation. *Biochem. Biophys. Res. Commun.* **387**, 381–386 (2009).

64. Casagrande, N. *et al.* CCR5 antagonism by maraviroc inhibits hodgkin lymphoma microenvironment interactions and xenograft growth. *Haematologica* **104**, 564–575 (2019).

65. Karnoub, A. E. *et al.* Mesenchymal stem cells within tumour stroma promote breast cancer metastasis. *Nature* **449**, 557–563 (2007).

66. Jiao, X. *et al.* CCR5 Governs DNA damage repair and breast cancer stem cell expansion. *Cancer Res.* **78**, 1657–1671 (2018).

67. Debré, P. *et al.* Increases Tumor Cell Infiltration Overexpression Delays Tumor Growth and Intratumoral CC Chemokine Ligand 5. *J Immunol Ref.* **173**, 3755–3762 (2021).

68. Dangaj, D. *et al.* Cooperation between Constitutive and Inducible Chemokines Enables T Cell Engraftment and Immune Attack in Solid Tumors. *Cancer Cell* **35**, 885-900.e10 (2019).

69. Romero, J. M. *et al.* A four-chemokine signature is associated with a T cell-inflamed phenotype in primary and metastatic pancreatic cancer. *Clin. Cancer Res.* clincanres.2803.2019 (2020). doi:10.1158/1078-0432.ccr-19-2803

70. Luo, J. *et al.* A protocol for rapid generation of recombinant adenoviruses using the AdEasy system. *Nat. Protoc.* **2**, 1236–1247 (2007).

71. He, T. C. *et al.* A simplified system for generating recombinant adenoviruses. in *Proceedings of the National Academy of Sciences of the United States of America* **95**, 2509–2514 (National Academy of Sciences, 1998).

72. D'Amico, L. *et al.* A novel anti-HER2 anthracycline-based antibody-drug conjugate induces adaptive anti-tumor immunity and potentiates PD-1 blockade in breast cancer. *J. Immunother. Cancer* **7**, 16 (2019).

73. flowCore: flowCore: Basic structures for flow cytometry data version 2.2.0 from Bioconductor. Available at: https://rdrr.io/bioc/flowCore/. (Accessed: 4th February 2020)

74. CATALYST: Cytometry dATa anALYSis Tools version 1.14.0 from Bioconductor. Available at: https://rdrr.io/bioc/CATALYST/. (Accessed: 4th February 2020)

75. GitHub - JinmiaoChenLab/Rphenograph: Rphenograph: R implementation of the PhenoGraph algorithm. Available at: https://github.com/JinmiaoChenLab/Rphenograph. (Accessed: 4th February 2020)

76. Levine, J. H. *et al.* Data-Driven Phenotypic Dissection of AML Reveals Progenitor-like Cells that Correlate with Prognosis. *Cell* **162**, 184–197 (2015).

77. CRAN - Package pheatmap. Available at: https://cran.r-project.org/web/packages/pheatmap/index.html. (Accessed: 4th February 2020)

78. GitHub - BIOP/ijp-kheops. Available at: https://github.com/BIOP/ijp-kheops. (Accessed: 14th May 2020)

79. GitHub - stardist/stardist: StarDist - Object Detection with Star-convex Shapes. Available at: https://github.com/stardist/stardist. (Accessed: 14th May 2020)

80. Bankhead, P. *et al.* QuPath: Open source software for digital pathology image analysis. *Sci. Rep.* **7**, (2017).

81. Samusik, N., Good, Z., Spitzer, M. H., Davis, K. L. & Nolan, G. P. Automated mapping of phenotype space with single-cell data. *Nat. Methods* **13**, 493–496 (2016).

82. Tirosh, I. *et al.* Dissecting the multicellular ecosystem of metastatic melanoma by single-cell RNA-seq. *Science (80-.).* **352**, 189–196 (2016).

83. Souza-Fonseca-Guimaraes, F., Cursons, J. & Huntington, N. D. The Emergence of Natural Killer Cells as a Major Target in Cancer Immunotherapy. *Trends in Immunology* (2019). doi:10.1016/j.it.2018.12.003